Minimal transition thresholds in plane Couette flow

Yohann Duguet, Antonios Monokrousos, Luca Brandt, and Dan S. Henningson

Additional information on Phys. Fluids

Minimal transition thresholds in plane Couette flow

Yohann Duguet,[1,a)] Antonios Monokrousos,[2,b)] Luca Brandt,[2,c)]
and Dan S. Henningson[2,d)]
[1]*LIMSI-CNRS, UPR 3251, F-91403 Orsay, France*
[2]*Linné Flow Centre, SeRc, KTH Mechanics, SE-100 44 Stockholm, Sweden*

Subcritical transition to turbulence requires finite-amplitude perturbations. Using a nonlinear optimisation technique in a periodic computational domain, we identify the perturbations of plane Couette flow transitioning with least initial kinetic energy for $Re \leq 3000$. We suggest a new scaling law $E_c = O(Re^{-2.7})$ for the energy threshold vs. the Reynolds number, in quantitative agreement with experimental estimates for pipe flow. The route to turbulence associated with such spatially localised perturbations is analysed in detail for $Re = 1500$. Several known mechanisms are found to occur one after the other: Orr mechanism, oblique wave interaction, lift-up, streak bending, streak breakdown, and spanwise spreading. The phenomenon of streak breakdown is analysed in terms of leading finite-time Lyapunov exponents of the associated edge trajectory. © *2013 AIP Publishing LLC*. [http://dx.doi.org/10.1063/1.4817328]

I. INTRODUCTION

It is well-established that most canonical wall-bounded shear flows can undergo transition to turbulence even in the absence of linear instability of the corresponding base flow. Either the base flow is linearly stable for all values of the Reynolds number Re, as is the case for the Hagen-Poiseuille flow (the flow inside a circular pipe driven by a pressure gradient) and plane Couette flow (the flow between two parallel plates moving in opposite directions), or it is linearly unstable for values of Re large compared to those where turbulence can be observed experimentally, as in the case of plane Poiseuille flow or boundary layer flows.[1,2] Transition to turbulence can be ensured by permanently modifying the system, hence turning the stable base flow into an unstable one. This can be achieved in practice by continuously forcing the flow or by randomly disturbing it on a long-time scale; for instance by placing finite-size obstacles, by continuous blowing or suction at the walls, or by using sufficiently rough surfaces. In this study, we will solely focus on situations where transition is triggered by imposing a velocity disturbance at a time $t = 0$, mainly because of the convenient, general, and well-posed mathematical framework associated with this initial value problem. In the "subcritical" regime, only some perturbations of sufficiently high initial energy can lead to turbulence. The first question that naturally arises is, for a given flow: what kind of perturbation can lead to transition with least initial energy? If transition is considered as undesirable (because of the increased wall friction), such a perturbation will be regarded as the most "dangerous" perturbation. If instead persisting turbulence is desired (for instance to achieve efficient mixing), such a perturbation would correspond to the energetically most "economical" way of inducing disorder in the system. In both cases, this "minimal perturbation" can be regarded as *optimal*. A second challenge arising is to identify the physical mechanisms by which it induces transition.

Together with the initial condition imposed at $t = 0$ and the boundary conditions, the mathematical system of equations governing the evolution of the velocity field is equivalent to an autonomous

---

a)Electronic mail: duguet@limsi.fr
b)Electronic mail: antonios@mech.kth.se
c)Electronic mail: luca@mech.kth.se
d)Electronic mail: henning@mech.kth.se

dynamical system of the form $\dot{x} = \mathcal{F}(x)$ in an infinite-dimensional phase space with a metric (in general understood as the total kinetic energy of a disturbance to the base flow) (see Fig. 1). The stable laminar flow, the only linearly stable fixed point $\mathcal{O}$ of the system, is in competition with a turbulent state $\mathcal{T}$ with strongly chaotic dynamics, which we assume to be an attractor for the parameter Re considered in our study. This competition implies that $\mathcal{O}$ has a basin of attraction $\mathcal{B}(\mathcal{O})$ delimited by its boundary Σ. Σ is an invariant set such that phase-space trajectories starting on Σ stay on it indefinitely.[3] Σ is often referred to as "the edge," while relative attractors sitting on Σ are referred to as "edge states." The problem of finding the minimal seed to turbulence is then equivalent to identifying a point M located arbitrarily close to Σ, yet outside $\mathcal{B}(\mathcal{O})$, such that the distance $d(\mathcal{O}, M)$ is minimal for the metric chosen.[4] The trajectory starting from M would by construction leave the neighbourhood of Σ and reach $\mathcal{T}$. How do M and $d(\mathcal{O}, M)$ evolve with increasing Re? More specifically, if we use as a metric the kinetic energy of perturbations, can we identify an exponent γ such that $d(\mathcal{O}, M) = E_c \sim Re^{-\gamma}$ for large Re?

Links between Reynolds number and transition to turbulence in wall-bounded shear flows have a long history. Reynolds[5] was probably first to point out the ratio of inertia to viscosity as the main parameter in his investigation of circular pipe flow. Despite the fact that the equations of motion are known, analytical derivation helps little in establishing thresholds. The most robust analytical result is the existence of a so-called "Energy Reynolds number" Re_E below which all perturbations return monotonically (in the L^2 norm) to the base flow. For plane Couette flow, $Re_E \approx 20.7$,[6] which is well below the experimental values of $Re_G \approx 320 - 370$ at which turbulence is observed in experiments.[7,8] Linearising the equations of motion around the base flow yields the classical Orr-Sommerfeld equation (when dealing with spanwise-independent perturbations) and the Orr-Sommerfeld-Squire system of equations for more generic three-dimensional perturbations.[9] However, the case of plane Couette flow (as that of circular pipe flow) is peculiar since no solution of the linearised system is found to grow exponentially in time, a result that holds for all values of Re.[10] In other words, the critical value Re_L for linear instability is here $Re_L = \infty$. Real transition occurs strictly between Re_E and Re_L. A first step towards untangling this apparent contradiction is to realise that the linearised operator L is non-normal, i.e., $LL^* \neq L^*L$. Still using the L^2 norm, non-normality permits transient algebraic growth of *some* perturbations for $Re > Re_E$ even in the linear regime,[11–13] while in the case $LL^* = L^*L$ we recover $Re_L = Re_E$.[14] An important consequence of the non-normality of L is that initially small perturbations can be amplified up to a level where nonlinearity can no longer be neglected. Another fact of importance is that, according to the Reynolds-Orr equation governing the evolution of the kinetic energy of a perturbation, only the linear terms of the Navier-Stokes equations contribute to the instantaneous change of the kinetic energy $E(t)$: because the nonlinear terms are energy-conserving, they can only contribute to energy transfer between various wavenumbers but do not produce energy themselves.[15] Following the success of the linearised approach, a vast number of methods have been developed to compute linearly optimal modes, those with an energy gain $G(T) = E(T)/E_0$ maximal for a given time T. Two-dimensional (i.e., spanwise-independent) optimal perturbations were identified in plane Couette flow as spanwise vortices leaning against the shear.[16] The only mechanism for energy growth identified here is the Orr mechanism,[17] where the shear essentially tilts the vortices into the direction of the flow, inducing mild transient growth of the energy while the total vorticity decays monotonically. Three-dimensional optimal modes are a much more efficient mechanism to extract energy from the base flow. The associated velocity field corresponds to exactly two-dimensional streamwise vortices (SV). The energy-extracting mechanism here is the lift-up mechanism,[15,18–21] where the vortices bring fast fluid from the boundaries to the bulk of the flow, where streamwise velocity is lower: the excess of streamwise velocity creates high-speed "streaks", i.e., fast lanes within the flow, while slow fluid advected towards the boundaries creates low-speed streaks. The gain in kinetic energy G scales like Re^2 and is thus strong at high values of Re.[15] The popularity of this linear mechanism is linked to the experimental evidence for both high and low-speed streaks in the near-wall region of all wall flows, with a mean spanwise spacing of $100h^+$ reasonably well reproduced by optimal modes.[22] Closer inspection of the growth of three-dimensional optimal modes also revealed the occurrence of the Orr mechanism.[23] A computationally powerful method to identify linearly optimal modes is to consider a Lagrangian $\mathcal{L}(\boldsymbol{q}, \boldsymbol{q}^*, \boldsymbol{q}_0, \boldsymbol{q}_0^*)$, where $\boldsymbol{q}$ is a state-space vector containing all physical

variables of interest, q_0 is its value at initial time $t = 0$, q^* is the vector adjoint to q with respect to $\mathcal{L}$. $\mathcal{L}$ is defined as the sum of an objective function to be maximised (typically the energy gain $G(T)$, where T is an additional parameter) and constraints defined using Lagrange multipliers.[13] An optimal vector q_0 is found iteratively by power iterations of the operator $e^{tL}e^{tL^*}$. Note that in parallel shear flows, the linearly optimal modes are streamwise-independent and cannot induce transition by themselves in a nonlinear setting: either noise or streamwise dependent "sub-optimal" modes have to be superimposed. Suppose now that optimal modes can be represented in the streamwise and spanwise directions using two fundamental wave numbers α and β, respectively, and denote $a = \alpha k_x$ and $b = \beta k_z$ integer multiples of α and β. An important class of sub-optimal modes corresponds to the subspaces spanned by (a, b) and $(a, -b)$, with $a, b \neq 0$. Two wave vectors defined by (a, b) and $(a, -b)$ can interact nonlinearly and exchange energy to feed the mode $(0, 2b)$, itself contained in the subspace of streamwise-independent modes, known to have the largest energy gain. This is the so-called Oblique Wave scenario.[24] Transition thresholds have been computed for both the streamwise vortices scenario (with the addition of numerical noise) and for the OW scenario in an almost-minimal periodic domain of plane Couette flow. The energy thresholds for the associated perturbations have been first reported[25,26] to scale Re^{-2}, and later $Re^{-2.5}$, considerably lower than the theoretical bound[25] $\gamma = 21/2$. These thresholds were later again refined using better numerical precision to $E_c = 4Re^{-2}$, the OW scenario needing a decade less in energy than the SV scenario to induce transition.[27] Note that we have here defined γ for the energy of perturbations rather than for the corresponding amplitude A_c considered by other authors. The same exponent $\gamma = 2$ was suggested analytically.[28] Waleffe and Wang, anticipating the concept of edge state,[29] also suggested[30] $\gamma = 2$. According to Waleffe's scenario, after transient growth by a gain $G = O(Re^2)$ the flow should equilibrate near a finite-amplitude state[31] that only asymptotically does not depend on Re. Other estimates for the energy threshold necessary for transition can be found in studies of circular pipe flow: a scaling $E_c = O(Re^{-2})$ was found experimentally by injecting fluid over a brief period of time.[32] It was confirmed both experimentally[33] and numerically[34] in pipe flow as well as in plane channel flow.[35] A steeper exponent $\gamma \approx 2.8$ was also identified in pipe flow by applying "push-pull" perturbations conserving the flow-rate,[36,37] a scenario confirmed later numerically.[34]

Nonlinear optimisation methods were developed only recently due to the large computational and storage cost associated with them.[38] It was pointed out that finite-amplitude perturbations maximising the energy gain after a finite time departed strongly from the linearly optimal modes associated to infinitely small initial energies.[38] The identification of "minimal seeds" was carried out in Blasius boundary layers[39,40] using an analogous objective function and again in pipe flow.[41] All those studies demonstrate that minimal seeds are spatially localised, delocalisation with time being an additional means for the perturbation of gaining kinetic energy. Monokrousos *et al.* (hereafter referred to as M11[42]) considered a different objective function, the time-integrated dissipation rate, rather than the usual energy gain $G(t)$. The original motivation stems out from a heuristic principle according to which wall-bounded turbulent flows (with time-invariant boundary conditions) correspond to statistically steady states maximising the total viscous dissipation under the constraint of a given mean velocity profile.[43] The outcome of the nonlinear optimisation in M11 is an initially spatially localised perturbation for each energy value ϵ_0 considered. Varying ϵ_0 allowed M11 to identify, for a given value of Re, the energy level below which the functional considered could no longer reach large values typical of turbulent episodes. Clearly, this critical energy should correspond to E_c provided the optimisation method returns the global optimum. It has been recently suggested, considering the same system of plane Couette flow, that optimising the energy gain G does not significantly alter the shape and energy of the corresponding minimal seed provided the optimisation is initiated for values of $\epsilon_0 < E_c$.[44] In what follows, we extend the approach initiated in M11 and consider varying Re, and we identify new nonlinearly optimised transition thresholds.

The goal of this study is to demonstrate the applicability of this numerical approach for the example of plane Couette flow in a moderate-size periodic domain. Once minimal perturbations are found and described, the optimal route to the turbulent state is described with an emphasis on the various phases of the process. A recent study has focused similarly on the transition mechanisms at low $Re = 400$ for large initial amplitudes.[45] Here we focus on the evolution from a minimal perturbation obtained at a large value of $Re = 1500$. As we shall see, along this special route,

several individual simple mechanisms can be identified, known from previous investigations under restrictive hypotheses such as linearity, two-dimensionality, or time-independence. This represents an opportunity to compare a transition mechanism in its globality to its separate building blocks, and to evaluate as well as discuss the validity of former approaches. Section II contains definitions, governing equations, and numerical techniques employed in this study. Section III introduces the optimisation procedure approach briefly exposed in M11 and focuses on the variation of minimal thresholds with Re . The description in Sec. IV unfolds the various mechanisms at play on the optimal trajectory. Section V contains a discussion of the results in relation with the recent literature on the topic.

A. Numerical method

Plane Couette flow (pCf) is the incompressible flow of a Newtonian fluid of kinematic viscosity ν, sheared between two infinite walls separated by a gap $2h$ and moving with velocities $\pm U$. Throughout this study, only non-dimensional variables will be used, where U is the unit for velocities, h is the unit for distances, and density is unity. The Reynolds number is classically defined as $Re := \frac{Uh}{\nu}$. We denote by x, y, and z the streamwise, wall-normal, and spanwise coordinates, respectively, and $\boldsymbol{e}_x$ is the streamwise unit vector. For the case of plane Couette flow, the base flow writes $\boldsymbol{U} = y\boldsymbol{e}_x$ and is associated with a homogeneous pressure field. The dynamics of a velocity-pressure perturbation $(\boldsymbol{u}, p)$ to the base flow $\boldsymbol{U}$ is ruled here by the perturbative nonlinear Navier-Stokes equations for the velocity field $\boldsymbol{u} = (u_x, u_y, u_z)$ and the pressure field p:

$$\frac{\partial \boldsymbol{u}}{\partial t} + (\boldsymbol{U} \cdot \boldsymbol{\nabla})\boldsymbol{u} + (\boldsymbol{u} \cdot \boldsymbol{\nabla})\boldsymbol{U} + (\boldsymbol{u} \cdot \boldsymbol{\nabla})\boldsymbol{u}$$

$$+ \boldsymbol{\nabla} p - \frac{1}{Re}\boldsymbol{\nabla}^2 \boldsymbol{u} = \boldsymbol{0}, \tag{1}$$

$$\boldsymbol{\nabla} \cdot \boldsymbol{u} = 0, \tag{2}$$

which can be written in the form

$$\partial_t \boldsymbol{u} - \boldsymbol{N}(\boldsymbol{u}) + \boldsymbol{\nabla} p = 0. \tag{3}$$

Perturbations in velocity are subject to the boundary conditions $\boldsymbol{u}(y = \pm 1) = 0$, while $\boldsymbol{U}(y = \pm 1) = \pm 1$.

Equations (1) and (2) are solved using direct numerical simulation in velocity-vorticity formulation[46] and the pressure term needs not be evaluated. The wall-normal velocity and the wall-normal vorticity are decomposed into N_y Chebyshev polynomials in the y direction, N_x Fourier modes in the x (streamwise) direction, and N_z Fourier modes in the z (spanwise) directions. The flow is advanced in time using an explicit fourth-order Runge-Kutta integrator with fixed timestep. The adjoint Navier-Stokes (introduced later) are integrated backwards in time using the same algorithm.

The flow is simulated inside a domain of size $\Omega = [0: L_x] \times [-1: 1] \times [-L_z/2: L_z/2]$ with periodic boundary conditions in x and z, see the sketch in Fig. 2. As in former studies,[26,27,42] we choose here $L_x = 4\pi$ and $L_z = 2\pi$. Accurate numerical resolution is used here, with $(N_x, N_y, N_z) = (128, 73, 64)$ for $Re = 750$ and 1500, $(160, 81, 96)$ for $Re = 2000$, and $(192, 81, 128)$ for $Re = 3000$.

We define the energy of perturbations to the base flow by

$$E = \frac{1}{4L_xL_z} \int_{\Omega} \sum_i |u_i|^2 dxdydz, \tag{4}$$

the viscous dissipation by

$$\mathcal{D} = 1 + \frac{1}{Re}\frac{1}{2L_xL_z} \int_{\Omega} \frac{\partial u_i}{\partial x_j}\frac{\partial u_i}{\partial x_j} dxdydz, \tag{5}$$
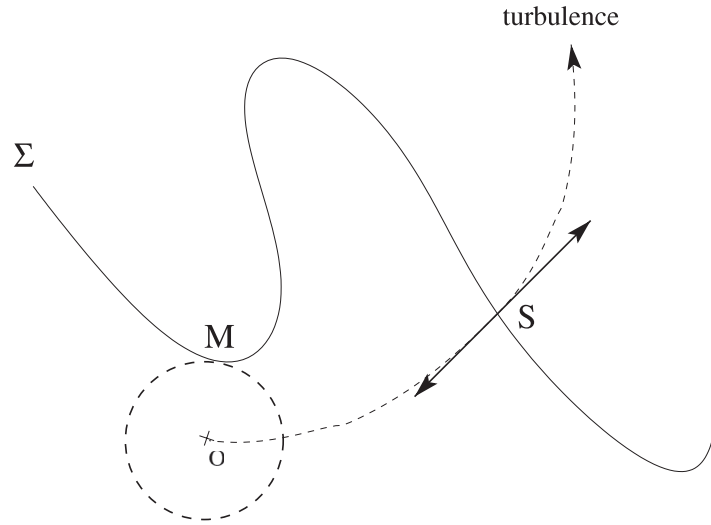
FIG. 1. Schematic view of the phase-space associated to the flow. O is the (stable) laminar state. Σ represents the laminar-turbulent boundary. The "edge state" S is the (unstable) asymptotical state on Σ. M is the minimal perturbation able to trigger transition to the turbulent state, i.e., the point on Σ closest to O in energy norm.

and the input energy by the wall shear by

$$\mathcal{I} = 1 + \frac{1}{2L_xL_z} \int_{x=0}^{x=L_x} \int_{z=0}^{z=L_z} \left(\frac{\partial u_x}{\partial y} |_{y=-1} + \frac{\partial u_x}{\partial y} |_{y=1} \right) dxdz. \tag{6}$$

The Reynolds-Orr equation writes in this case

$$\frac{dE}{dt} = \mathcal{I} - \mathcal{D}. \tag{7}$$

II. NONLINEAR OPTIMISATION PROCEDURE

The Lagrangian approach is used here where an objective function $\mathcal{J}$ is chosen on physical grounds and constraints are specified in the form of Lagrange multipliers. We are looking for stationary points of the Lagrange functional $\mathcal{L}$, where optimality is fulfilled with respect to the various design variables. The direct variables in the optimisation are contained in a large vector $\tilde{u}$ containing the perturbation velocity field $u(x, t)$ and the pressure field $p(x, t)$, and is considered in a suitable space of functions defined on $\Omega \times [0: T]$. In order to keep notations compact, we will use the following metrics:

$$< \cdot, \cdot >_{\Omega} = \frac{1}{2L_xL_z} \int_{x=0}^{x=L_x} \int_{z=0}^{z=L_z} \int_{y=-1}^{y=1} (\cdot, \cdot) dxdydz, \tag{8}$$

$$\ll \cdot, \cdot \gg = \int_0^T < \cdot, \cdot >_{\Omega} dt. \tag{9}$$

Obvious dynamical constraints are:
(i) $\partial_t u - N(u) - \nabla p = 0$
(ii) $\nabla \cdot u = 0$
both to be satisfied at each point in Ω and each time $t \in]0: T[$.

Let us define formally functionals acting on the space of velocity/pressure fields and corresponding to the initial energy

$$\epsilon : \tilde{u} \to E = \frac{1}{2} < u(t = 0), u(t = 0) >_{\Omega} \tag{10}$$

and to the total time-averaged dissipation

$$\mathcal{J} : \tilde{\boldsymbol{u}} \to \frac{1}{T} \int_0^T \mathcal{D}(t)dt, \tag{11}$$

where $\mathcal{D}(t)$ is the viscous dissipation defined in Eq. (5).

Note that time-integration of Eq. (7) between $t = 0$ and T yields

$$\frac{E(T) - E(0)}{T} = \frac{1}{T} \int_0^T \mathcal{I}dt - \mathcal{J},$$

which provides a link between our objective function $\mathcal{J}$ and the energy gain $G(T)$ considered by previous authors:

$$\mathcal{J} = \left(\frac{1}{T} \int_0^T \mathcal{I}dt \right) - \frac{E(0)}{T}(G - 1). \tag{12}$$

The term containing $(G - 1)$ in Eq. (12) becomes negligible for large T since G is always bounded in a nonlinear context. The main advantage of using the present objective function $\mathcal{J}$ over G is that it is not an instantaneous quantity defined at a single time. It contains instead an average contribution of positive $D(t)$ at all times, and saturates for large T in a monotonous way. In contrast to $G(t)$, it neither undergoes rapid variations nor pronounced overshoots when approaching the edge (see Sec. V B in Ref. 27) or the turbulent regime. Also, maximising $\mathcal{J}$ amounts to maximising the area between 0 and $D(t) > 0$ in the interval $[0 : T]$. This implies for $\epsilon_0 > E_c$ that the algorithm seeks the trajectory reaching high dissipation in the *fastest* way.

We will impose the additional constraint on $\boldsymbol{u}(\boldsymbol{x}, t)$:
(iii) the energy of the perturbation at $t = 0$ is set to ϵ_0, i.e.,

$$\epsilon(\tilde{\boldsymbol{u}}) = \epsilon_0. \tag{13}$$

The scalar Lagrangian functional $\mathcal{L}$ is introduced in the form

$$\mathcal{L}(\boldsymbol{X}) = \mathcal{J}(\tilde{\boldsymbol{u}}) - \ll \boldsymbol{v}, \partial_t \boldsymbol{u} - N(\boldsymbol{u}) + \nabla p \gg$$
$$- \ll q, \nabla \cdot \boldsymbol{u} \gg - \lambda(\epsilon(\tilde{\boldsymbol{u}}) - \epsilon_0), \tag{14}$$

where $\boldsymbol{X} = (\tilde{\boldsymbol{u}}, \boldsymbol{v}, q, \lambda)$ is a compact variable containing $\tilde{\boldsymbol{u}}$, as well as all Lagrange multipliers (or adjoint variables): the adjoint velocity field $\boldsymbol{v}(\boldsymbol{x}, t)$, the adjoint pressure field $q(\boldsymbol{x}, t)$, and a scalar coefficient λ. By construction, derivation of the Lagrangian with respect to the dual variables $\boldsymbol{v}$, $\boldsymbol{q}$, and λ yields, respectively

$$\partial_{\boldsymbol{v}}\mathcal{L} = -(\partial_t \boldsymbol{u} - N(\boldsymbol{u}) + \nabla p), \tag{15}$$

$$\partial_q\mathcal{L} = -\nabla \cdot \boldsymbol{u}, \tag{16}$$

$$\partial_\lambda\mathcal{L} = -(\epsilon(\tilde{\boldsymbol{u}}) - \epsilon_0). \tag{17}$$

The state $\boldsymbol{u}$ maximising $\mathcal{J}$ under all constraints is solution of $\partial_{\boldsymbol{X}}\mathcal{L} = 0$. We thus also need to evaluate $\partial_{\tilde{\boldsymbol{u}}}\mathcal{L}$. We use integration by parts to evaluate

$$\partial_{\boldsymbol{u}}\mathcal{J} = -\frac{1}{T\,Re}\nabla^2 \boldsymbol{u}. \tag{18}$$

For the term including the time-derivative $\partial_t \boldsymbol{u}$, we again use integration by parts

$$\ll \boldsymbol{v}, \partial_t \boldsymbol{u} \gg = [< \boldsymbol{v}, \boldsymbol{u} >_\Omega]_0^T - \ll \partial_t \boldsymbol{v}, \boldsymbol{u} \gg . \tag{19}$$

Evaluating derivatives of $\mathcal{L}$ with respect to "columns" $\tilde{\boldsymbol{u}}(t)$ for a given $t \in]0 : T[$, we note that $\partial_{\boldsymbol{u}}\mathcal{L} = 0$ and $\partial_p\mathcal{L} = 0$ imply respectively:[44]

$$\frac{\partial \boldsymbol{v}}{\partial t} + N^\dagger(\boldsymbol{v}, \boldsymbol{u}) - \nabla q - \frac{1}{T\,Re}\nabla^2 \boldsymbol{u} = \boldsymbol{0}, \tag{20}$$

$$\nabla \cdot \boldsymbol{v} = 0, \tag{21}$$

where

$$N^{\dagger}(\boldsymbol{v}, \boldsymbol{u}) = \partial_{x_j} u_j v_i - v_j \partial_{x_i} u_j - \partial_{x_j} U_j v_i$$
$$- v_j \partial_{x_i} U_j + \frac{1}{Re} \partial_{x_j}^2 v_i \tag{22}$$

is a quadratic form with respect to both $\boldsymbol{u}$ and $\boldsymbol{v}$. Because it also depends on $\boldsymbol{u}$, the fields $\boldsymbol{u}(x, t)$ need be stored at all times for the later time-integration of Eq. (20). As for the direct pressure term in Eq. (1), the dual pressure term $-\nabla q$ in Eq. (20) need not be evaluated since this equation will be time-stepped in the velocity-vorticity formulation.

This is valid for all times t except at $t = 0$ and $t = T$ where the velocity fields $\boldsymbol{u}_0 = \boldsymbol{u}(\boldsymbol{x}, t = 0)$ and $\boldsymbol{u}_T = \boldsymbol{u}(\boldsymbol{x}, t = T)$ appear explicitly out of spatial integrals in Eqs. (14) and (19):

$$\partial_{\boldsymbol{u}_0} \mathcal{L} = -\lambda \boldsymbol{u}_0 + \boldsymbol{v}(\boldsymbol{x}, t = 0), \tag{23}$$

$$\partial_{\boldsymbol{u}_T} \mathcal{L} = -\boldsymbol{v}(\boldsymbol{x}, t = T). \tag{24}$$

Equating the expression in Eq. (24) to zero would lead to the compatibility conditions

$$\boldsymbol{u}_0 = \frac{1}{\lambda} \boldsymbol{v}(\boldsymbol{x}, t = 0), \tag{25}$$

$$\boldsymbol{v}(\boldsymbol{x}, t = T) = 0. \tag{26}$$

Starting from a velocity field $\boldsymbol{u}_0^{(k)}$, $k \geq 0$ which constitutes an initial guess for the optimal corresponding to an imposed value of ϵ_0, we use the classical forward-backwards iterative method to obtain the next guess $\boldsymbol{u}_0^{(k+1)}$. Starting from the initial condition $\boldsymbol{u}(t = 0) = \boldsymbol{u}_0^{(k)}$, Eq. (3) is integrated from $t = 0$ to $t = T$. At $t = T$, the compatibility condition in Eq. (26) is used to initialise $\boldsymbol{v}(t = T)$. Equation (20) is then integrated backwards in time until $t = 0$ (only backwards integration is possible because of the negative diffusion in Eq. (22)). If the algorithm has converged, all derivatives in $\partial_X \mathcal{L}$ vanish. Far enough from convergence, this is true except for $\partial_{\boldsymbol{u}_0} \mathcal{L}$ which will progressively be brought to zero using a relaxation technique

$$\boldsymbol{u}_0^{(k+1)} = \sigma \boldsymbol{u}_0^{(k)} + (1 - \sigma)(\partial_{\boldsymbol{u}_0} \mathcal{L})^{(k)}, \tag{27}$$

where $\sigma = 0.95$ is used and $(\partial_{\boldsymbol{u}_0} \mathcal{L})^{(k)}$ is evaluated as a function of $\boldsymbol{u}_0^{(k)}$ and $\boldsymbol{v}_0^{(k)}$ using Eq. (25). When reinitialising k by $k + 1$, the normalisation constraint in Eq. (13) is eventually used to fix the value of the multiplier λ. The main computational difficulty of the algorithm concerns the heavy storage of the snapshots of $\boldsymbol{u}$ during forward time-stepping, later used to compute the forcing terms for backwards time-stepping the dual evolution in Eq. (20). Note the lighter storage alternative by the method of "checkpointing".[41]

The algorithm is initialised by a field $\boldsymbol{u}_0^{(k=0)}$ corresponding to random divergence-free noise for values of ϵ_0 far above the expected threshold, and by linear optimals[47] for small ϵ_0. When approaching $\epsilon_0 = E_c$ from above, the result of one optimisation is used as input for the next one, until ϵ_0 is low enough for relaminarisation (hence low values of the objective function $\mathcal{J}$) to be inevitable.

For small ϵ_0 convergence towards the linear optimal state is as expected fast.[38,41,44] On the contrary, for too large values of ϵ_0, the algorithm wanders around without converging. Being interested in threshold values for ϵ_0, we actually take this as an advantage because the algorithm avoids stagnating near local minima of $\mathcal{J}$ potentially located in $\mathcal{B}(\mathcal{O})$, and hence does identify turbulent episodes. Satisfactory convergence was obtained for $\epsilon_0 \gtrsim E_c$, judging from several norms (such as $\mathcal{J}$, energies or $||\boldsymbol{u}||_\infty$) and from the shape of the final state which is independent of both k and T (provided $T \geq 300$, see M11). We did not investigate convergence properties further, the most important outcome of this optimisation being the identification of at least one episode of high dissipation as long as $\epsilon_0 > E_c$. We note that the exact value $\epsilon_0 = E_c$, by construction, would
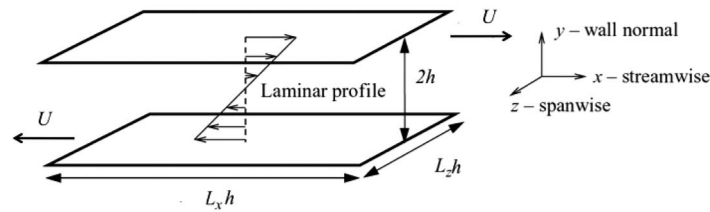
FIG. 2. Geometry and notations for plane Couette flow.

correspond to the state M being *exactly* on Σ (see Fig. 1). The associated trajectory hence cannot trigger turbulence in a finite time, whereas any arbitrarily small and well-oriented deviation from M can. This constitutes a singular limit for the optimisation procedure: the integration time T diverges as ϵ_0 approaches the exact value of E_c from above. Fortunately, in practice a two-digit accuracy for E_c is within reach with $T \leq 400$.

III. RESULTS

A. Nonlinear transition threshold

By varying the initial energy ϵ_0 for a given value of Re, and listing whether turbulent (high values of the dissipation) episodes are encountered either as end-results or as transient visits during the optimisation procedure, it is possible to find the energy level E_c below which no transition to turbulence can occur. The accuracy of the procedure is limited by the number of values of ϵ_0 swept through, which if large can lead to enormous computational costs. Nevertheless, a two-digit accuracy on E_c is within reach. Here we are interested in the scaling of E_c with respect to increasing values of Re, and we have hence repeated the estimation of E_c for four values of $Re = 750, 1500, 2000,$ and 3000, ensuring that the numerical resolution was well adapted to each case. The minimal threshold energy $E_c = f(Re)$ is shown in Fig. 3. A clear power-law scaling $Ec = O(Re^{-\gamma})$ emerges with $\gamma \approx 2.7$, which is valid over the range $Re \in [750: 3000]$. It is steeper than all estimates given so far, where γ was closer to 2 (or equivalently $A_c = O(Re^{-1})$ in amplitude). Not only the exponent but also the total energy is also lower than in former studies, meaning that the minimal perturbations found here have lower energy than all previously found perturbations. For comparison, the threshold curve obtained for oblique waves, associated with the exponent $\gamma = 2$ and computed in the same computational box,[27] is also shown in Fig. 3.

B. Optimal initial conditions

We show the various minimal perturbations identified for $Re = 750, 1500, 2000,$ and 3000 in Fig. 4. Here we use the same plotting scheme as M11 for better comparison, i.e., we plot iso-contours of the streamwise velocity perturbation u_x corresponding to 0.65 times the maximum. Despite small discrepancies due to the difficulty of landing exactly on Σ, it is striking that all the perturbations identified here belong to a unique class of minimal perturbations, characterised by a staggered pattern of alternatively positive and negative velocities, inside a three-dimensionally localised region. All perturbations are oriented in a direction pointing against the shear, suggesting that the Orr mechanism will be at play at early times, as will be verified later. There is a trend towards stricter localisation as Re increases, suggesting some sort of self-similarity. However, this is here difficult to confirm quantitatively and would probably, even if physically plausible, be affected by the periodic boundary conditions. It is also interesting to compare to the minimal field identified in Ref. 27 (Fig. 5) using a small projection basis: only the localisation properties seem to differ. We can thus reasonably expect analogies between the route to turbulence associated to either perturbation.
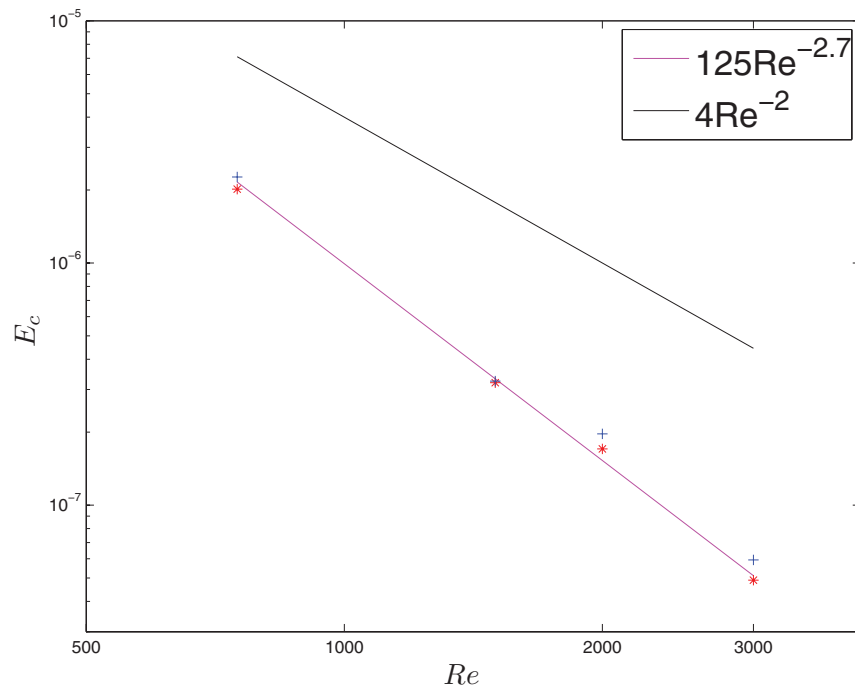
FIG. 3. Energy threshold E_c vs. Re for $Re = 750, 1500, 2000,$ and 3000. Stars represent the largest tested value of E_0 below which transition never occurs, while crosses represent the smallest tested value of E_0 for which transition occurs at least once. The fit $125Re^{-2.7}$ (pink) is compared to the fit $4Re^{-2}$ (black) obtained for the Oblique Wave scenario for the same computational box (data from Ref. 27).
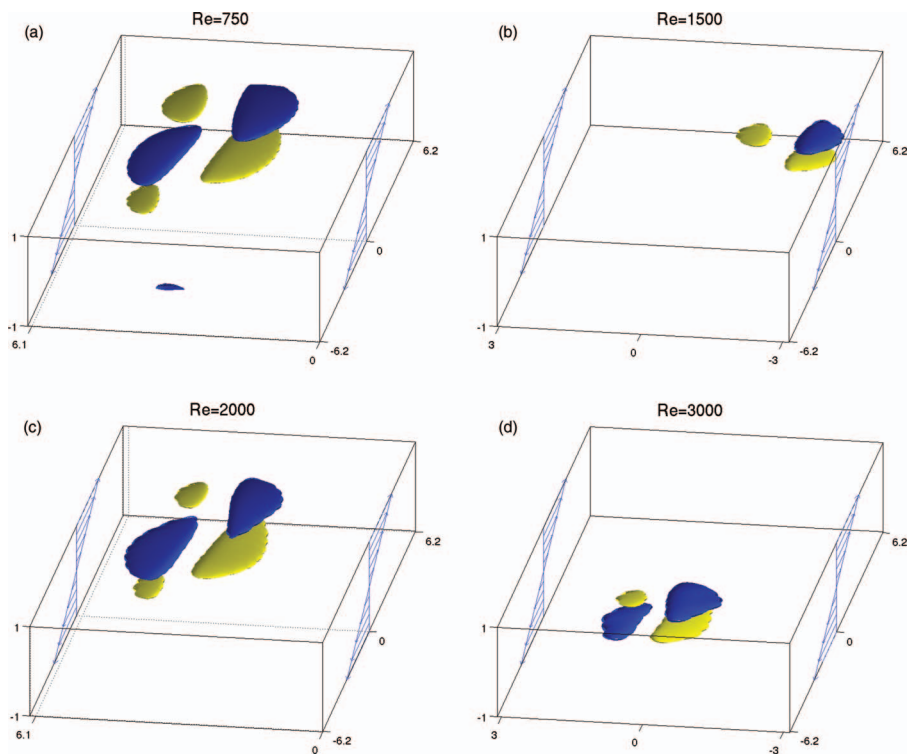
FIG. 4. Nonlinear optimal conditions for $Re = 750, 1500, 2000,$ and 3000. Iso-contours of the streamwise velocity perturbation u' corresponding to $\pm 0.65 \max u_x$. Blue arrows represent the base flow $U_x = y$.
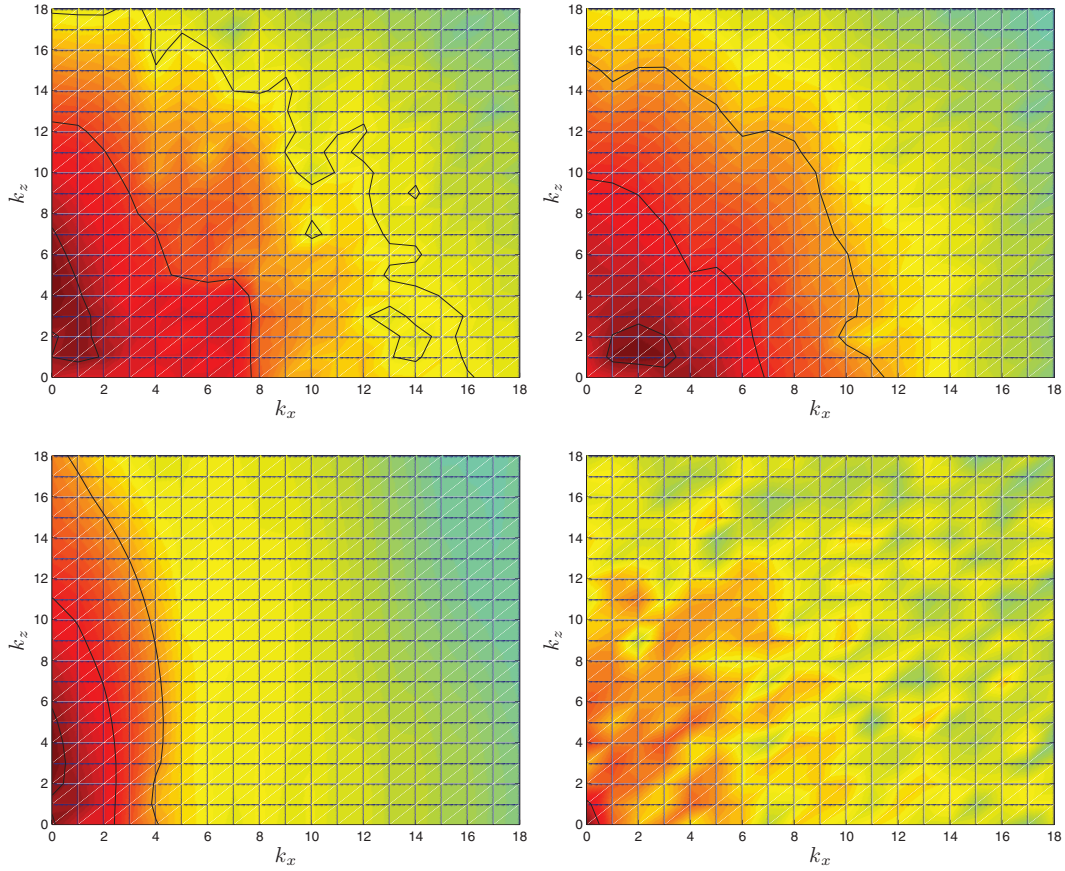
FIG. 5. Spectral distribution of kinetic energy $\log e(k_x, k_z)$ normalised by its maximum, for the minimal seed for $Re = 1500$ at $t = 0$, $t = 10$, $t = 100$, and $t = 180$ (from left to right and from top to bottom). The iso-contours correspond to $E/\max(E) = 10^{-1}, 10^{-5}$, and 10^{-10}.

IV. OPTIMAL PATH TO TURBULENCE FOR $Re = 1500$

A. Spectral portrait

We choose here to focus on the temporal evolution from the minimal seed identified for $Re = 1500$. We begin by analysing the spectral energy distribution of Fourier modes corresponding to the minimal seed. We define the spectral distribution of kinetic energy $e(k_x, k_z)$ by

$$e(k_x, k_z) = \int_{y=-1}^{y=1} \left(|\hat{u}_x|^2 | + |\hat{u}_y|^2 + |\hat{u}_z|^2 \right)_{(\alpha k_x, \beta k_z)} dy, \tag{28}$$

where (α, β) is the fundamental wavevector $(2\pi/L_x, 2\pi/L_z)$. Figure 5 shows the spectrum corresponding to the minimal seed at $t = 0$ (top left panel), as well as its temporal evolution at later times $t = 10$, 100, and 180 (where the flow is turbulent). At $t = 0$, the most energetic modes are of the type $(k_x, k_z) = (0, n)$ but their immediate followers are $(1, \pm 1)$, $(2, \pm 1)$, $(3, \pm 1)$, $(4, \pm 1)$, and $(1, \pm 2)$, i.e., oblique modes. Little energy is also contained in the $k_x = 0$ modes and it increases with $|k_z|$, consistently with the spanwise localisation, while very little energy is contained in the $k_z = 0$ subspace. This clearly indicates that oblique modes dominate the spectrum of the initial condition, and that the oblique wave scenario, involving transfer of energy towards the $k_x = 0$ axis, is expected to dominate the modal interactions for $t > 0$. This is verified at $t = 100$ where most of the energy is concentrated in a stripe around $k_x = 0$, including to a lesser extent modes with $k_x = 1, 2$, that involve all wave numbers $k_z \leq 20$. This is interpreted as nonlinear transfer of energy from all $k_x \neq 0$ modes towards the dominant structures that are almost streamwise-independent.[24]
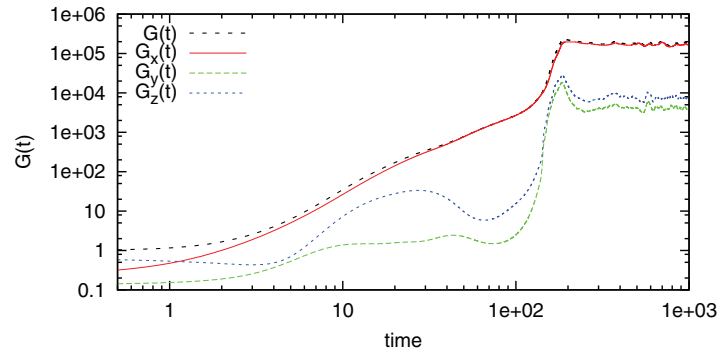
FIG. 6. Time evolution of gains $G(t)$ (black dashed online), $G_x(t)$ (red online), $G_y(t)$ (green dotted online), and $G_z(t)$ (blue dashed online).

Figure 6 shows the energy gain G vs. time, i.e., the kinetic energy normalised by its initial value. Also shown are the energy gains per velocity component G_x, G_y, and G_z, defined by

$$G_x(t) = \frac{1}{2}\frac{u_{rms}^2(t)}{E(0)}, G_y(t) = \frac{1}{2}\frac{v_{rms}^2(t)}{E(0)}, G_z(t) = \frac{1}{2}\frac{w_{rms}^2(t)}{E(0)}, \tag{29}$$

where for simplicity, we define $u_{rms} = <u_x\mathbf{e}_x, u_x\mathbf{e}_x>_\Omega$, $v_{rms} = <u_y\mathbf{e}_y, u_y\mathbf{e}_y>_\Omega$, and $w_{rms} = <u_z\mathbf{e}_z, u_z\mathbf{e}_z>_\Omega$, with $\mathbf{e}_i$ the unit vector in the direction $i = x, y, z$. Those gains are defined such that $G = G_x + G_y + G_z$. Figure 6 shows a clear uninterrupted growth of the kinetic energy until $t \approx 200$, followed by a stabilisation of the average gain around $G \approx 2.10^{+5}$, indicating that the statistically steady turbulent regime has been reached. As expected, the turbulent regime shows irregular fluctuations of the energy. Comparison of the various components building the gain makes it clear that although not initially significant, the contribution of the streamwise velocity component G_x dominates from $t \geq 10$ onwards. The gains G_y and G_z, despite growing in magnitude from $t \approx 30 - 40$ onwards, are not important until a dramatic increase occurs near $t \approx 150$, followed slightly later by a faster increase of G_x. Note that the approach to the average turbulent equilibrium is characterised by a strong overshoot of both G_y and G_z that is less pronounced for G_x. All these phases of the energy growth correspond to various instability mechanisms to which the rest of this paper is devoted.

In order to highlight the various instability phenomena occurring on the corresponding path towards the turbulent state, we chose to mainly focus on the evolution of the velocity field in *physical* space. Three planes turn out to give an insightful representation of the dynamical evolution of the flow. We use here the following notations: p_z represents a plane with $z = cst$ (here taken as $z = -1.57$), p_x a plane with $x = cst$ (here $x = 0$), and p_y a plane with $y = cst$ (here $y = -0.5$). As will become clear in the following, p_z is best associated to the description of the Orr mechanism, p_x to the lift-up effect, and p_y to streak breakdown. It is noteworthy how those three stages of the transition seem to occur one after the other rather than all combined together. How much this is a feature of the transition induced by the minimal seed only remains to be verified.

B. Orr mechanism

The linear Orr mechanism,[17] also termed Reynolds stress mechanism,[20] expresses the tilting of spanwise vorticity by the mean flow. It is most easily understood by assuming two-dimensionality (here, spanwise invariance) and small perturbation amplitude. The equation for the vorticity perturbation ω_z is obtained by taking the z-component of the curl of the linearised version of Eq. (1):

$$(\partial_t + U(y)\partial_x - Re^{-1}\nabla^2)\omega_z = u_y U'', \tag{30}$$

where for plane Couette flow $U(y) = y$ and $U'' = 0$. Equation (30) is linear in ω_z and constitutes the main mechanism for energy growth for the two-dimensional linear optimal modes. A common
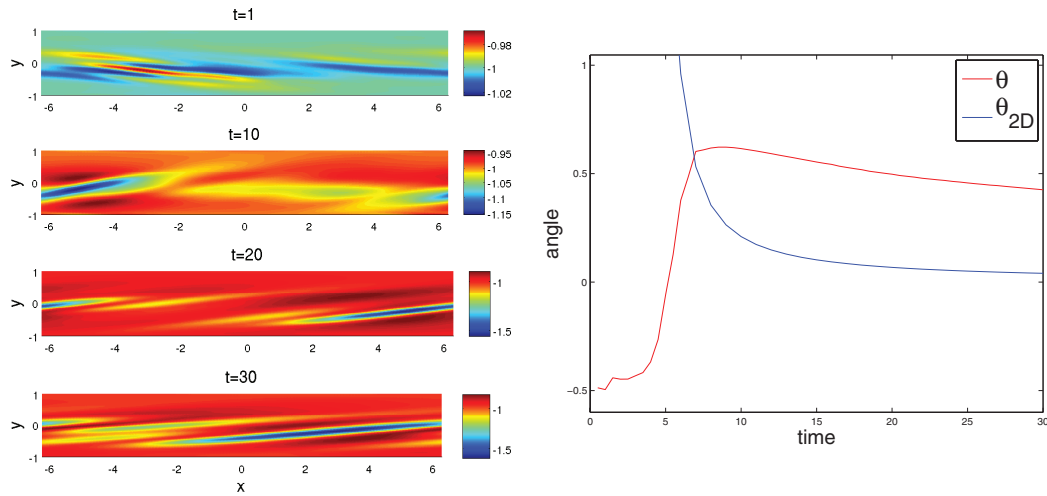
FIG. 7. Left: Spanwise vorticity ω_z in the plane $p_z : z = -\frac{\pi}{2}$ at times $t = 1, 10, 20,$ and 30. Right: Angle θ computed using the second eigenvalue of the Hessian tensor of ω_z at the minimum of $\omega_z|_{p_z}$ vs. time. Comparison with theoretical two-dimensional angle $\theta_{2D}(t)$ for a Kelvin wave solution.

interpretation is that any initial patch of perturbation spanwise vorticity is sheared and hence tilted into the direction of the shear,[48] until viscosity acts against further stretching. This non-normal mechanism is responsible for initial energy growth in two dimensions. Using the notation $\boldsymbol{r} = (x, y)$, Eq. (30) admits a Kelvin mode solution

$$\omega_z(t) = A(t)e^{i\boldsymbol{k}(t)\cdot\boldsymbol{r}},$$

where

$$\frac{dA}{dt} = -\frac{|\boldsymbol{k}|^2}{Re}A$$

and

$$\boldsymbol{k}(t) = (k_x(t^*), k_y(t^*) - k_x(t^*)(t - t^*)),$$

where t^* is some arbitrary time. We deduce that the angle $\theta_{2D}(t)$ between the vorticity sheet and the streamwise direction should vary such as

$$\theta_{2D}(t) = \arctan \frac{|k_x(t^*)|}{|k_y(t^*) - k_x(t^*)(t - t^*)|}. \tag{31}$$

Choosing t^* such that $k_y(t^*) = 0$ (when the sheet is flipped into the direction of the shear) is convenient and yields

$$\theta_{2D}(t) = \frac{\pi}{2} - \arctan(t - t^*), \tag{32}$$

which is independent of k_x. We demonstrate here that the early development of the minimal disturbance computed for $Re = 1500$ corresponds to the Orr mechanism. Figure 7 (left) focuses on the plane p_z (i.e., $z = -1.57$) and shows that the spanwise vorticity is progressively tilted in the direction of the background shear, more evidently for $t \in [10 : 30]$. For each time t, we have identified the minimum value $\omega_z(x, y)$ over p_z. The Hessian matrix of $\omega_z(x, y)$ is approximated by finite differences, then its smallest eigenvalue and the associated eigenvector $\boldsymbol{V} = (V_x, V_y)$ are extracted. An angle $\theta(t)$ is defined here by $\theta = \arctan V_y/V_x$, and is interpreted as the tilting angle of the spanwise vorticity disturbance by the spanwise shear in the plane $z = cst$.

After an initial reorientation phase, $\theta(t)$ decreases monotonically to zero as $\theta_{2D}(t)$ does in Eq. (32). A value of t^* is chosen when flipping of the sheet occurs with respect to the wall-normal axis, i.e., $t \approx 5.3$, which allows to set the missing parameter in Eq. (32). The angle θ and its theoretical
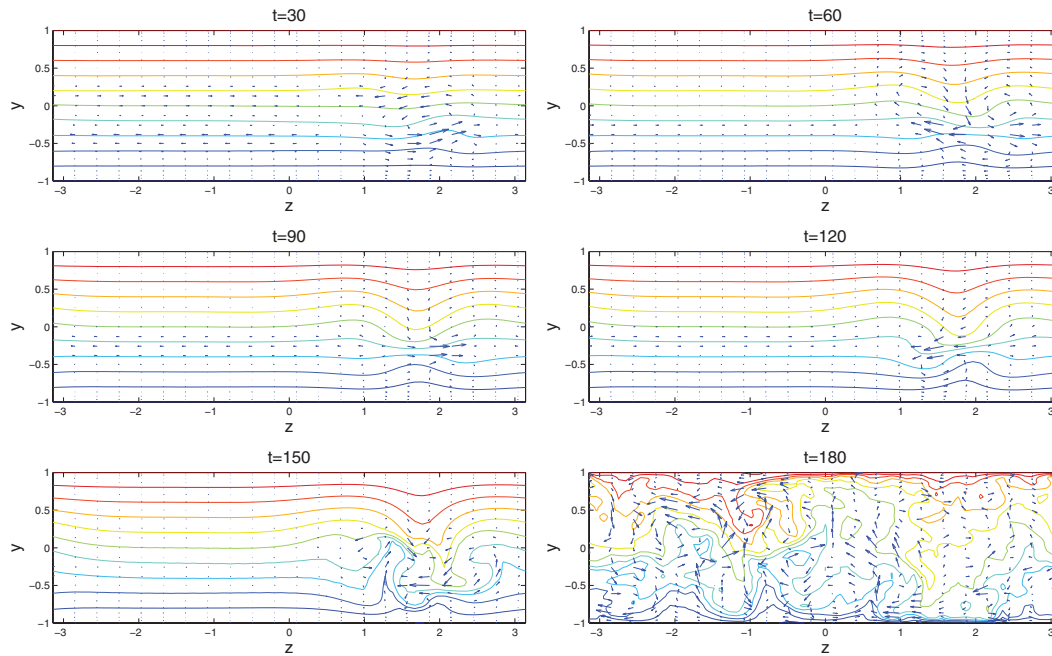
FIG. 8. Cross-sections of the velocity field in the plane p_x: $x = 0$, for times $t = 30$, 60, 90, 120, 150, and 180. Contours: iso-levels of $U_x + u_x$; arrows: (u_y, u_z) vectors.

counterpart θ_{2D} are shown vs. time in Fig. 7 (right). The qualitative match is good for $t \gg t^*$. The quantitative match is less satisfying, as expected: the true disturbance is actually three-dimensional and involves many oblique modes with $\beta \neq 0$. Nonlinear interaction of all these modes is expected to affect the evolution of the angle θ. Besides, it is expected that the formation of wiggling streaks documented next prevents $\theta(t)$ from approaching zero as it would in the two-dimensional case.

C. Lift-up mechanism

We consider here the velocity field associated to the full velocity field (base flow + perturbation) in the plane p_x: $x = 0$ (the choice for $x = 0$ is arbitrary). The iso-contours of the streamwise velocity are reported in Fig. 8 along with the cross-flow vectors in the same plane. Flat equidistant iso-contours at $t = 0$ correspond to $U + u_x = y$, i.e., the initial departure from the base flow has no streamwise component, whereas modulations in z indicate alternance of low-speed and high-speed streaks. From Fig. 8, it is striking that a localised waviness of the iso-contours starts to manifest itself from $t = 30$ on around $z \approx 2$. This undulation is connected to the existence of an unsteady vortex in the plane p_x.

The mechanism for the emergence of the streaks is best understood when considering the two-dimensional (streamwise-independent) version of Eq. (1). Projection in the streamwise direction yields

$$\left(\partial_t + u_y \partial_y + u_z \partial_z - Re^{-1}\left(\partial_y^2 + \partial_z^2\right)\right)(U_x + u_x) = 0. \tag{33}$$

Equation (33) represents the linear advection of the total streamwise velocity $(U_x + u_x)$ by the cross-stream flow (u_y, u_z). The linearity of Eq. (33) with respect to u_x results here from the assumption of x-invariance only, not from any assumption that u_x should be small. If additionally the cross-stream components u_y and u_z are assumed to be small quantities, their linear evolution decouples from Eq. (33) and they undergo slow viscous decay on a time scale $O(Re)$. Before diffusion terms become important, Eq. (33) behaves as a transport equation, so that advection manifests itself in the plane p_x by a local displacement of the iso-contours of $U_x + u_x$ from their initial position with instantaneous cross-stream velocity (u_y, u_z). This distortion produces local amplification of u_x up to

a magnitude $O(Re)$ times that of the transverse flow. The perturbation energy is rapidly dominated by the streamwise component u_x while the cross-stream components decay viscously, and the transient energy gain is at most $O(Re^2)$.[15] Once the cross-stream gradients of u_x become too steep as an effect of distortion, diffusion terms take over. All three components of the perturbation eventually decay to zero with decay rate $O(Re^{-1})$, if no forcing or no nonlinear feedback is present and maintains them to a finite-amplitude level.[31] This linear mechanism describes the linear dynamics of three-dimensional linear optimal modes, where the transverse motion (u_y, u_z) is associated precisely to an x-independent streamwise vortex.[20]

In our nonlinear simulation in turn, it was already clear from Fig. 6 that the streamwise velocity component u_x dominates the energy growth from $t \approx 15$ on, suggesting that streamwise streaks develop rapidly through the lift-up mechanism. The wall-normal displacement of the iso-contours of $U_x + u_x$ from their corresponding laminar position increases with time until $t \approx 150$, confirming that the streaks are continuously growing in magnitude. The mechanism discussed in the preceding paragraph is evident here, with the exception that the flow is far from being x-independent, as attested by the unsteadiness of the cross-stream vortex. As pointed out recently,[49] the emergence of x-dependent streaks (or in other words bent streaks characterised by $k_x \neq 0$) can be traced back to an initial excess of spanwise velocity u_z with respect to the linearly optimal $k_x = 0$ scenario. This is indeed the case here as can be seen from Fig. 6, where initially $G_z(t = 0)$ is larger than both $G_x(t = 0)$ and $G_y(t = 0)$. Initial conditions with an excess of initial w_{rms} can shortcut the linearly optimal scenario by inducing a bent streamwise vortex (i.e., with $k_x \neq 0$), that later develops streaks via lift-up. However, these streaks are now bent and the initial energy needed to reach them can be lower than the initial energy required to make the flow transition using nearly-x-independent streamwise vortices.[49] This phenomenon is most likely at play here given the bent structure of the streaks displayed in Fig. 10 in the p_y plane. However, as we will now show, the streaky field is not only x-dependent, but also shows asymmetry with respect to the mid-plane $y = 0$.

Shortly before $t = 150$, a strong ejection occurs towards negative values of y, indicating an instability of the streak. Turbulence develops locally first, before spreading in z. The instability process can be more clearly unfolded using Fig. 9, which displays the minimum y_{min} and maximum y_{max} of the y-coordinate over the $u = 0$ iso-surface with respect to time. For laminar flow, $y_{min} = y_{max} = 0$ whereas $y_{min} < 0 < y_{max}$ in the presence of streaks. Figure 9 shows that both y_{min} and y_{max} slowly increase with time from $t \approx 30$ on, i.e., after the Orr mechanism has occurred. The growth of y_{max} is monotonous while the decrease of y_{min} occurs faster and features temporal oscillations of period $t_S \approx 20 - 25h/U$. The sudden breakdown is visible for y_{min} at $t = 140$, while y_{max} shows a dramatic increase only from $t \approx 160$ on. We deduce from Fig. 9 that the low-speed streak in the lower-half of the domain has gone unstable first, after supporting growing oscillations (already visible via the oscillations of the cross-flow vortex in Fig. 8). The asymmetry in y suggests that a $k_x \neq 0$ perturbation has travelled along a straight streak with absolute phase velocity $L_x/t_S \approx 0.5 - 0.6U$. This finite-amplitude undulation is convected towards decreasing x by the negative mean velocity corresponding to values of $y < 0$, until it undergoes a dramatic instability. The fact that the breakdown of that bent streak occurs first for negative y motivates the choice for the plane p_y with $y = -0.5$.

D. Streak breakdown

Figure 10 shows the velocity field in the $y = -0.5$ plane. As previously suggested, a spanwisely localised zone is easily located, containing a high-speed streak and a low-speed streak side by side, with a weak undulation in x of wavelength exactly L_x. The iso-contours of v in that plane closely follow those of u until $t \approx 140$. At $t \approx 142$, the iso-contours of v display a shorter-wavelength mode at the junction between the low-speed streak and the high-speed streak.[50] It is characterised by two small zones of down-welling and up-welling motion (respectively negative and positive values of v) of streamwise extent ≈ 1. Once this disturbance appears, the streak pattern is strongly affected, justifying the name "streak breakdown," though formally regions of high and low streamwise velocity can still be defined. The later evolution of that disturbance follows a two-step process: until $t \approx 160$, more and more up/down-welling zones appear at the former location of the streak and
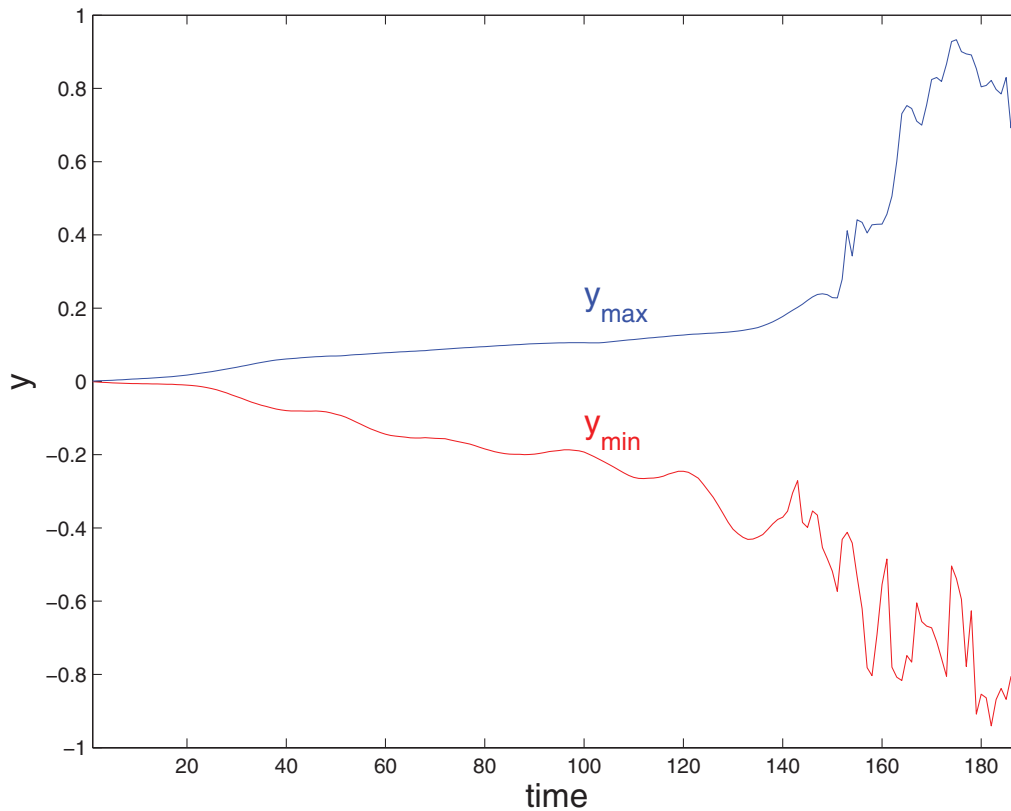
FIG. 9. Wall-normal positions of the maxima and minima of the iso-surface $U_x + u_x = 0$ vs. time.

disorder progressively spreads in the x direction. In a second phase, starting at ≈ 165, disorder ("turbulence") starts to spread in the spanwise direction until the whole computational domain is filled by unsteady motion.

E. Edge trajectory and streak breakdown

The instability of streaks and its relation to transition to turbulence has been discussed in many studies. However, almost all former studies are based on linear stability analysis of a base flow that remains to be properly defined. For instance, it was often assumed that streaks saturate at a steady amplitude after the linear transient growth stage.[51] While this approximation provides one with a simple steady base flow to linearise around, it is clear that in general no such steady base flow exists. Besides, the linear instability of the flow around this saturated base flow was often examined under the additional implicit assumption that the underlying mechanism is inviscid.[51,52] These studies lead to a qualitatively correct classification of the various symmetries of the streak instability modes, consistent with experimental observations. The search for linear optimal perturbations was generalised by seeking secondary optimal perturbations that are able to extract energy from an unsteady base flow,[53] where the unsteady base flow considered corresponds to the transiently growing streaks excited by linearly optimal modes. The dynamics associated to linearly optimal modes is physically relevant only for very low initial amplitudes and is not necessarily concerned with transition itself.

In the present study, the edge trajectory $t(M)$ starting from the minimal perturbation M is a much better suited candidate as an *unsteady* base flow. We recall that an edge trajectory is a trajectory evolving on the invariant separatrix Σ, that asymptotically reaches a relative attractor called edge state. The minimal perturbation M is never found exactly but approximated in practice by a state M' with energy ϵ_0 slightly larger than E_c. As shown in Fig. 10, the transitioning trajectory $t(M')$
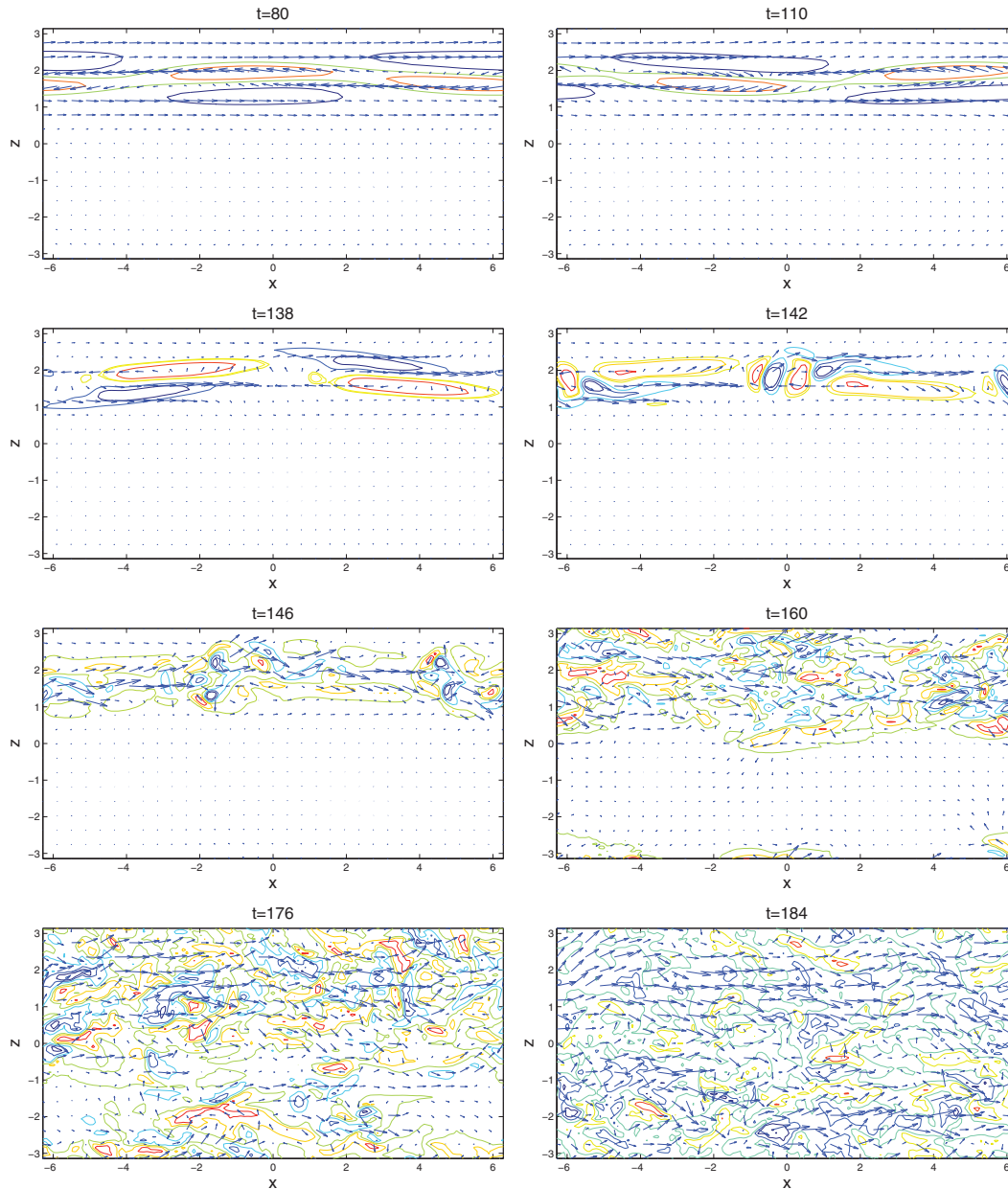
FIG. 10. Velocity field in the plane p_y: $y = -0.5$. u_y: colours, (u_x, u_z): arrows. Iso-contours of u_y normalised by their maximum, where $\max u_y = 0.0055$ ($t = 80$), 0.0117 ($t = 110$), 0.052 ($t = 138$), 0.1023 ($t = 142$), 0.2329 ($t = 146$), 0.3333 ($t = 160$), 0.3273 ($t = 176$), and 0.5473 ($t = 184$).

starting from M' shadows the trajectory $t(M)$ for a finite time just before streak breakdown occurs (at $t \approx 142$ in the case of Fig. 10). A better approximation M' of M (i.e., with ϵ_0 even closer to E_c) would shadow the edge trajectory $t(M)$ for a longer time, and subsequently streak breakdown would occur at a later time. For arbitrary high accuracy in the procedure used to approximate M, the departure from the neighbourhood of the reference edge trajectory (i.e., "streak breakdown") can occur at any time. The instability to be quantified, independently of the accuracy of the procedure, is hence the local rate of divergence of trajectories initially infinitesimally close to this edge trajectory, measured for all initial times over the reference trajectory.

Natural tools for such an investigation are the finite-time Lyapunov exponents[54] and the associated finite-time Lyapunov perturbations. These exponents λ^T measure the exponential rate at

which two neighbouring phase-space trajectories diverge one from another in a time T, while the associated perturbations describe the principal directions associated with this divergence. For any state $\boldsymbol{u}$ in $\mathcal{B}(\mathcal{O})$, $\lim_{t \to +\infty} |\boldsymbol{u}(t) + \boldsymbol{\delta u}(t)| = 0$ for any small perturbation $\boldsymbol{\delta u}$, and hence $\lambda_{max}^{T} = 0$ for sufficiently large T. In turn, for $\boldsymbol{u} \in \Sigma$, it is by definition possible to find infinitesimal perturbations to $\boldsymbol{u}$ leading to either of the two attractors, hence $\lambda_{max}^{T} \neq 0$. Crossing Σ from below thus marks the onset of positive Lyapunov exponents. While the determination of the full Lyapunov spectrum of a given phase-space trajectory is a heavy task in high dimension, estimating the leading Lyapunov exponent and the associated Lyapunov perturbation with a finite time horizon, and as a function of the initial time, is more tractable.[29] Moreover, when studying wall-bounded shear flows in the $Re \to \infty$ limit, the determination of the largest Lyapunov exponent is counterintuitively simpler than for finite Re, since one unstable Lyapunov exponent must dominate over all others. It can be justified as follows: the chaotic dynamics on Σ can be regarded as a sequence of transient approaches to the neighbourhood of some unstable states belonging to Σ, each with two unstable eigenvalues or more.[55] From previous studies,[56,57] we know that the associated unstable eigenvalues λ_i, $i = 1, 2, \ldots$ are always such that $\lambda_i = O(Re^{-\alpha_i})$, with $0 < \alpha_1 < \alpha_2 \leq \ldots$. When Re becomes large, $|\frac{\lambda_2}{\lambda_1}| \to 0$. The perturbation associated with λ_1 would thus rapidly dominate the divergence of nearby trajectories and this trend gets more pronounced with increasing Re. This justifies *a priori* the assumption made earlier. Note in passing that the condition $|\frac{\lambda_2}{\lambda_1}| \ll 1$ has been suggested[58] as a condition for Σ to be non-fractal, so that Σ can indeed safely be regarded as a smooth manifold only for high enough Re. Note that in the extreme case where the edge state is a simple state (steady state, travelling wave, or a periodic orbit) with only one unstable eigenvalue λ_1, the largest Lyapunov exponent λ_{max} on Σ must coincide with λ_1.

We describe now how the leading finite-time Lyapunov exponent is estimated numerically. The edge trajectory $\boldsymbol{u}_{edge}(t)$ associated with M (or rather its numerical approximation) is determined using a classical bisection. At any given time t_0 along this edge trajectory, we apply a small perturbation $\boldsymbol{\delta u}(t_0)$ so that the trajectory starting from $\boldsymbol{u}_{edge}(t_0) + \boldsymbol{\delta u}(t_0)$ reaches the turbulent attractor in a finite time. If the real part of the Lyapunov spectrum is dominated at each time by one single exponent λ, it is expected that $\boldsymbol{\delta u}(t)$ becomes rapidly aligned with the associated Lyapunov vector. At a finite time $T \gg 1$, we can thus define an approximation to the leading finite-time Lyapunov exponent by

$$\lambda^T(t_0) = \frac{1}{T} ln \left(\frac{|\boldsymbol{\delta u}(t_0 + T)|}{|\boldsymbol{\delta u}(t_0)|} \right). \tag{34}$$

In order to make sure that the perturbation $\boldsymbol{\delta u}(t_0)$ makes the flow transition rather than relaminarise, we use the initial condition $\boldsymbol{u}(t_0) = (1 + \varepsilon)\, \boldsymbol{u}_{edge}(t_0)$, with small $\epsilon > 0$ (typically 10^{-3}). The perturbed trajectory turns out to be a by-product of the bisection algorithm used to determine $\boldsymbol{u}_{edge}$.

The procedure is shown in Fig. 11. The nonlinear optimal trajectory $t(M')$ described earlier, the associated edge trajectory $t(M)$ and the evolution of several small perturbations to $t(M)$ are shown vs. time using the quantity w_{rms}. Figure 12 shows the value of $\lambda^T(t_0)$ vs. initial time t_0. Clearly,
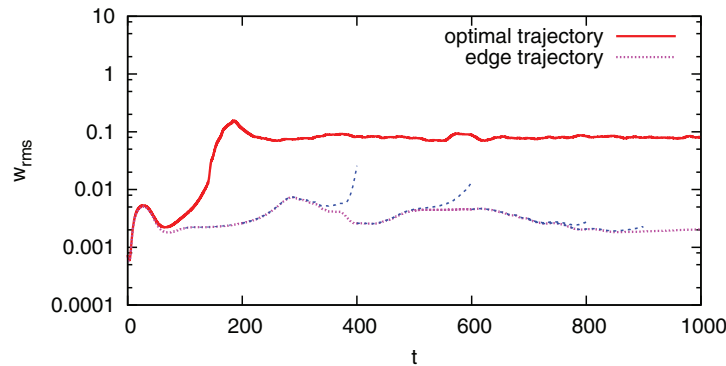
FIG. 11. $w_{rms}(t)$ for the turbulent trajectory (solid/red) starting from the minimal seed, the edge trajectory (dotted/purple) starting from the rescaled minimal seed. Evolution of initially small deviations from the edge trajectory (dashed/blue).
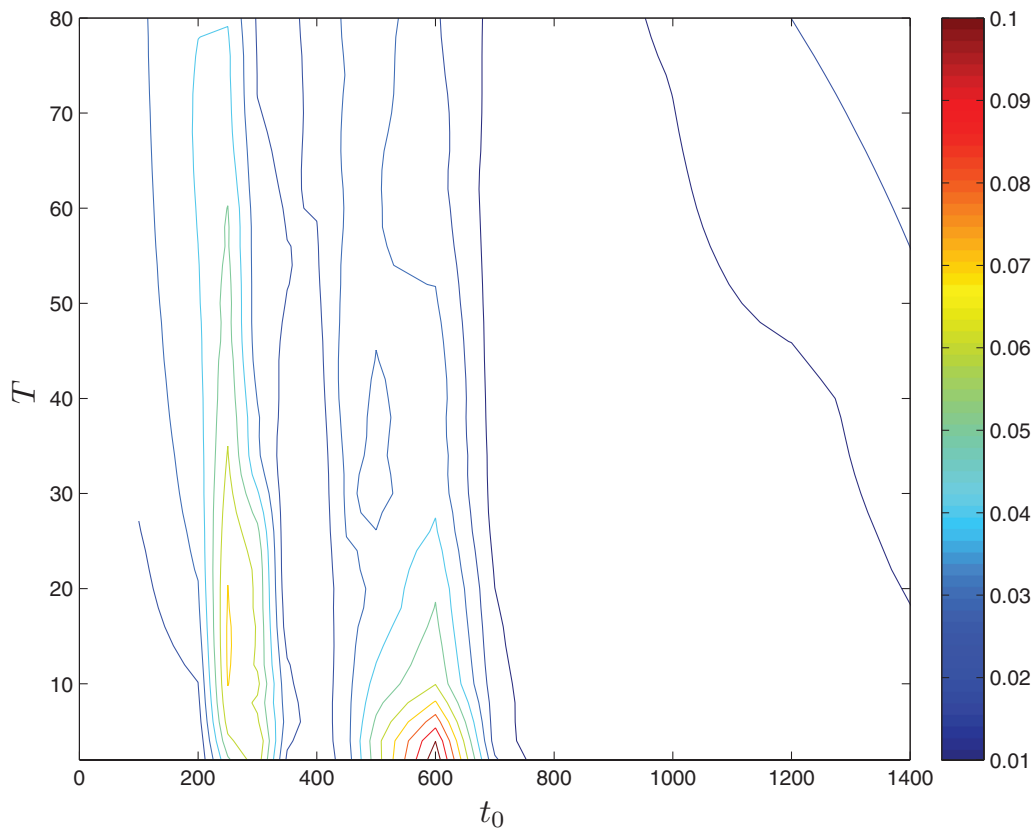
FIG. 12. Finite-time Lyapunov exponent $\lambda^T(t_0)$ as function of t_0 and T along the edge trajectory.

$\lambda^T(t_0)$ varies with the initial time t_0, especially for short time-horizons $T \leq 20$. Such time horizons are shorter than the typical time scale $O(100)$ over which the base flow varies. It is thus justified to regard the exponential growth of $\delta\boldsymbol{u}(t)$ as an instantaneous instability of the flow field $\boldsymbol{u}(t_0)$. $\lambda^T(t_0)$ experiences a strong increase (about 10 times in magnitude) for $t_0 \approx 250 - 350$, before it relaxes again, and then experiences a second strong increase for $t_0 \approx 450 - 600$. One can wonder which physical property of the instantaneous field $\boldsymbol{u}(t_0)$ is responsible for the variations in the growth rates $\lambda^T(t_0)$. A recent study[49] has suggested that streak breakdown could be caused not only by a large streak amplitude (measured by u_{rms}), but also by its *bending* if u_{rms} is low enough. Streak bending was shown[49] to be well quantified by the instantaneous value of w_{rms}. Figure 13 shows the value of $\lambda^T(t_0)$ for $T = 10$ vs. instantaneous values of both $u_{rms}(t_0)$ and $w_{rms}(t_0)$. It is clear from Fig. 13 that the states on the edge trajectory associated with the largest growth rates correspond to extreme values of either $w_{rms}(t_0)$ (for $t_0 \approx 300$) or $u_{rms}(t_0)$ (for $t_0 \approx 500$). A one-to-one correlation between $\lambda^T(t_0)$ and some other well-defined quantity does not emerge clearly from the data. We confirm that the growth rate of disturbances leaving the edge trajectory depends non-trivially on both the instantaneous streak amplitude and the bending of the streaks.

Three-dimensional representations of the reference edge trajectory (iso-levels of u_x), with the Lyapunov perturbations (iso-levels of u_y) superimposed, are displayed in Fig. 14 for relatively short time horizons $T \leq 20$. The edge trajectory consists for all times t_0 of an isolated high-speed streak sandwiched between two uneven low-speed streaks, localised in z with a very weak undulation travelling towards negative x. They look similar to the states observed along the nonlinear route for $30 < t < 140$ (see Fig. 10), except that the streaks are no longer of finite length, excluding now an instability due to streak collision.[50] All perturbations identified for $200 \leq t_0 \leq 1200$ and $T \leq 20$ are mainly localised in the neighbourhood of the streaks, in the high-shear region between the low-speed and high-speed streaks. This is most evident for the perturbation shown in Fig. 14 (top right) for
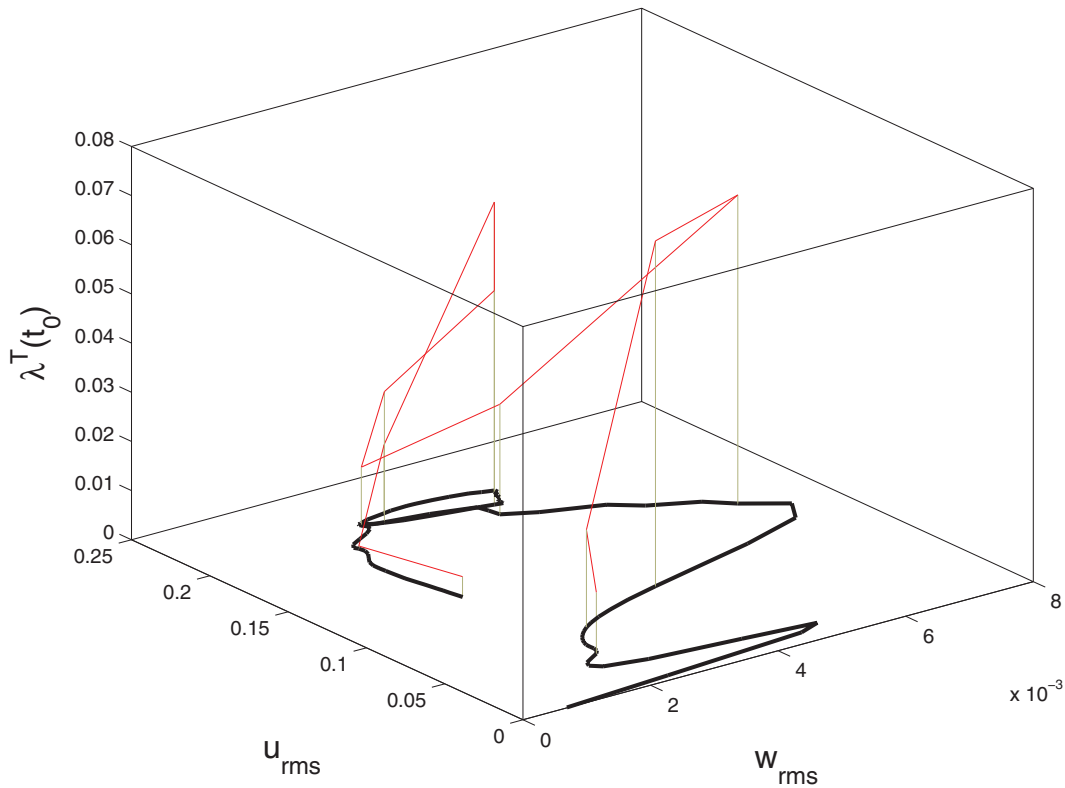
FIG. 13. Thin line (red): Finite-time Lyapunov exponent $\lambda^T(t_0)$ as a function of $u_{rms}(t_0)$ and $w_{rms}(t_0)$ for $T = 10$ and $t \leq 1000$. Thick line (black): Projection of the edge trajectory in the plane (u_{rms}, w_{rms}).

$t_0 = 500$. This particular perturbation corresponds to the largest value of $\lambda^T(t_0)$ identified from Fig. 12 near $t_0 \approx 500$, i.e., when the streaks are most unstable. The short-time Lyapunov perturbation consists then of alternated perturbations with a clear sinuous structure and a dominant $k_x = 3$ mode. At other times t_0 characterised by lower $\lambda^T(t_0)$, the Lyapunov perturbations seem supported by lower k_x modes, e.g., $k_x = 1$ at $t_0 = 200$ and 1200, and $k_x = 2$ at $t_0 = 700$. Note that the preferred instability mode at $t_0 = 700$ has a varicose structure rather than a sinuous one. The sinuous or varicose nature of such instabilities points towards an inviscid instability due to the spanwise shear,[59] sinuous modes having been identified as the preferred instability mode of both tubular and bent streaks in previous studies on linear streak instabilities.

F. Spreading mechanism

As visualised in Fig. 10, the transition from an ordered flow, containing one single localised low-speed streak (near $t \approx 100$), to the fully turbulent flow maximising the dissipation rate occurs as a two-step process: (i) streak breakdown resulting in a localised streak with wild local fluctuations and (ii) rapid spanwise spreading of the turbulent flow. The Lyapunov perturbations described in Fig. 14 are predominantly localised in the region between the streaks and not at the border between streaks and laminar flow. This excludes the hypothesis that the motion of the front is directly related to the instability modes of the edge state, and thus justifies a two-step process. Unlike streak breakdown, analysis of spanwise spreading in terms of Lyapunov instabilities is one step harder because the flow is already in a locally turbulent regime and the number of positive Lyapunov exponents is now much larger than for edge-restricted trajectories. While an asymptotic estimate spanwise front velocity of 0.08 can be found using a modelling strategy[60] for large Re, a detailed statistical analysis[61] is needed for a correct estimation of spanwise front velocities in such a streamwisely minimal domain. The computational box used here is too narrow for a detailed study of the contamination
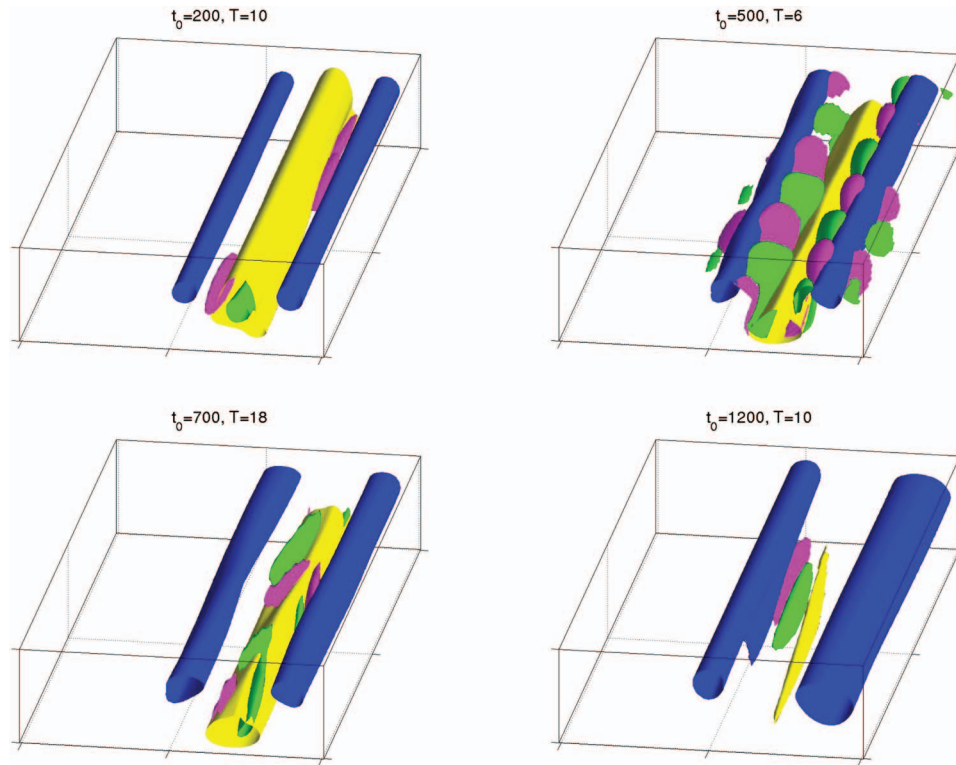
FIG. 14. Wall-normal velocity isosurface $|u_y| = C_y \max u_y$ of the Lyapunov perturbation (pink: $u_y > 0$, green: $v_y < 0$). Streamwise perturbation velocity isosurface $|u_x| = C_x \max u_x$ of the edge trajectory (yellow: $u_x > 0$, blue: $u_x < 0$). From left to right, top to bottom: (a) $t_0 = 200$, $T = 10$; (b) $t_0 = 500$, $T = 6$; (c) $t_0 = 700$, $T = 18$; and (d) $t_0 = 1200$, $T = 10$. Same isometric view as Fig. 4. $C_x = 0.55$ except for $t_0 = 200$: $C_x = 0.3$ and $t_0 = 1200$: $C_x = 0.9$, $C_y = 0.4$ except for $t_0 = 1200$ where $C_y = 0.7$.

process of laminar by turbulent flow. The important lesson is that front velocities (i) involve complex streak bursting events near the laminar-turbulent interfaces and (ii) should be seen as stochastic quantities that are not available by simple linearisation around a laminar unperturbed base flow. For both streamwisely and spanwisely localised turbulent spots, we refer to previous numerical[62] and experimental work[7,8] performed for $Re \leq 1000$.

V. CONCLUSIONS

A nonlinear optimisation procedure,[42] where the objective function is the time-averaged viscous dissipation, has been used to determine a critical scaling $E_c = O(Re^{-\gamma})$ for minimal disturbances to plane Couette flow. We have identified an exponent $\gamma \approx 2.7$, significantly larger than previous estimates for plane Couette flow. The main difference compared to previous minimal candidates is here the spanwise localisation of the flow before streak breakdown occurs. There is little doubt that allowing for a longer computation domain would also reveal more pronounced streamwise localisation and probably yield a refined value for γ. Yet this remains extremely costly today given the lengths needed to observe localisation of edge states,[63,64] that most likely vary such as $L_x \sim O(Re)$. The exponent γ identified here is close to that identified experimentally in cylindrical pipe flow using constant mass flux injectors.[37] The route from the minimal perturbation identified for $Re = 1500$ towards the turbulent attractor has been investigated in detail. A two-dimensional $(\sqrt{E_u}, \sqrt{E_{cf}})$ phase space projection of this transitioning trajectory, along with the corresponding edge trajectory, is shown in Fig. 15, where $E_u = \frac{1}{2}u_{rms}^2$ and $E_{cf} = \frac{1}{2}(v_{rms}^2 + w_{rms}^2)$. It is interesting to compare Fig. 15 to the introductory sketch in Fig. 1 to appreciate the validity of the speculated picture.
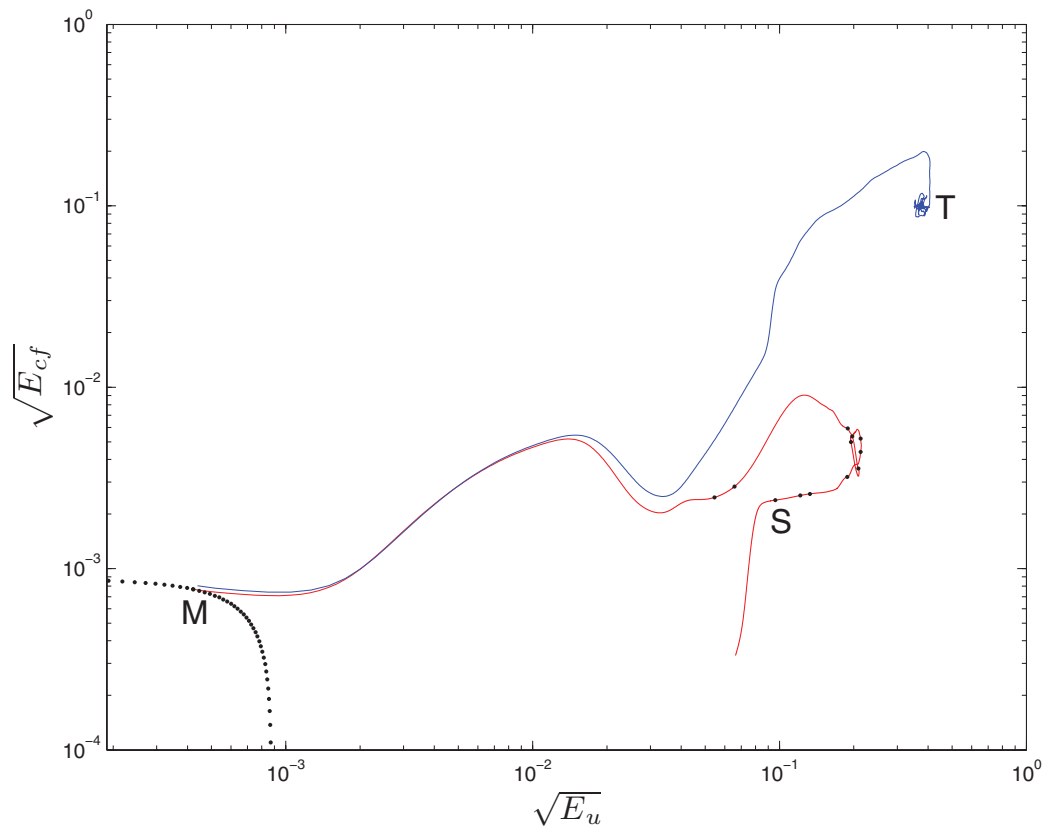
FIG. 15. $(\sqrt{E_u}, \sqrt{E_{cf}})$ projection of phase space with the nonlinear optimal trajectory (blue), the associated edge trajectory (red), and $\epsilon_0 = E_c$ (black dots) for $Re = 1500$. To be compared with Fig. 1.

We focused more specifically on the dynamics along the transitioning trajectory in *physical* space. Interestingly, the description provided here reviews *all* the mechanisms identified independently from each other and they seem to proceed nearly one after another, which facilitates greatly the analysis: (1) Orr mechanism (tilting of vorticity by the ambient shear), (2) nonlinear modal interactions of oblique modes favouring the emergence of bent streaks, (3) lift-up mechanism (advection of streamwise velocity by the cross-stream flow) leading to a spanwisely localised streak, (4) streak breakdown, and (5) stochastic spanwise spreading. Interestingly, while the whole phenomenon of transition, and obviously turbulence itself, are fully nonlinear mechanisms, this optimal route to turbulence can be decomposed formally into a sequence of separate mechanisms. Most of the mechanisms producing energy growth are describable using classical linearisation approaches: Orr and lift-up mechanisms are essentially linear advection mechanisms. Oblique wave interaction is essentially nonlinear but occurs at constant energy, since nonlinear terms are energy-conserving. Streak breakdown has been here revisited as a linear instability mechanism of a generically unsteady edge trajectory. It is linked to an inflectional instability due to the shear between low and high-speed streaks, favouring either sinuous or sometimes also varicose modes. This study also indicates that the instability growth rate and the bending of the streaks can be positively correlated. This observation has important implications for flow control: any external action aiming at keeping the wall shear stress low (at least at the level of edge states) should damp the instability of streaks. Hence a powerful strategy is to act against their bending, i.e., to favor streak elongation. The efficiency of streak elongation for control strategies is attested by many examples, such as applying a streamwise magnetic field (in the case of electrically conducting fluids) or adding a small amount of polymers in the flow. A less bent streak on the edge is by definition still unstable, but on a slower time scale. The efficiency of the control strategy will thus be improved if it can produce elongation over a time

scale τ such that $\tau \ll 1/\lambda^\tau(t_0)$. Only the final stage of transition, namely the spatial spreading of turbulence, is possibly unrelated to any linear mechanisms, where at this point one enters the territory of spatio-temporal intermittency.[61] We strongly hope that all these observations will be useful for better modelling of transition to turbulence in all subcritical flows as well as for designing realistic control strategies.

ACKNOWLEDGMENTS

[1] P. G. Drazin and W. H. Reid, *Hydrodynamic Stability* (Cambridge University Press, Cambridge, 1985).

[2] P. Manneville, "Modelling the direct transition to turbulence," in *Non-Uniqueness of Solutions to the Navier-Stokes Equation and Their Connection With Laminar-Turbulent Transition*," edited by T. M. Mullin and R. R. Kerswell (Springer-Verlag, Dordrecht, 2005), pp. 1–33.

[3] B. Eckhardt, T. M. Schneider, B. Hof, and J. Westerweel, "Turbulence transition in pipe flow," Annu. Rev. Fluid Mech. **39**, 447–468 (2007).

[4] C. Cossu, "An optimality condition on the minimum energy threshold in subcritical instabilities," C. R. Mec. **333**, 331–336 (2005).

[5] O. Reynolds, "An experimental investigation of the circumstances which determine whether the motion of water shall be direct or sinuous and of the law of resistance in parallel channels," Philos. Trans. R. Soc. London **174**, 935–982 (1883).

[6] D. D. Joseph, *Stability of Fluid Motions* (Springer-Verlag, Berlin, 1976).

[7] N. Tillmark and P. H. Alfredsson, "Experiments on transition in plane Couette flow," J. Fluid Mech. **235**, 89–102 (1992).

[8] O. Dauchot and F. Daviaud, "Finite amplitude perturbation and spots growth in plane Couette flow," Phys. Fluids **7**, 335 (1995).

[9] P. J. Schmid and D. S. Henningson, *Stability and Transition in Shear Flows* (Springer-Verlag, New York, 2001).

[10] V. A. Romanov, "Stability of plane-parallel Couette flow," Funct. Anal. Appl. **7**, 137–146 (1973).

[11] L. Boberg and U. Brosa, "Onset of turbulence in a pipe," Naturforsch., A: Phys. Sci. **43**, 697–726 (1988).

[12] L. N. Trefethen, A. E. Trefethen, S. C. Reddy, and T. Driscoll, "Hydrodynamic instability without eigenvalues," Science **261**, 578–584 (1993).

[13] P. J. Schmid, "Nonmodal stability theory," Annu. Rev. Fluid Mech. **39**, 129–162 (2007).

[14] D. S. Henningson and S. C. Reddy, "On the role of linear mechanisms in transition to turbulence," Phys. Fluids **6**, 1396–1398 (1994).

[15] S. C. Reddy and D. S. Henningson, "Energy growth in viscous channel flows," J. Fluid Mech. **252**, 209–238 (1993).

[16] B. F. Farrell, "Optimal excitation of perturbations in viscous shear flow," Phys. Fluids **31**, 2093–2102 (1988).

[17] W. M. F. Orr, "The stability or instability of the steady motion of a perfect liquid or of a viscous liquid," Proc. R. Ir. Acad. A, Math. Phys. Sci. **27**, 9–138 (1907).

[18] T. Ellingsen and E. Palm, "Stability of linear flow," Phys. Fluids **18**, 487 (1975).

[19] M. T. Landahl, "A note on an algebraic instability of inviscid parallel shear flows," J. Fluid Mech. **98**, 243–251 (1980).

[20] K. M. Butler and B. F. Farrell, "Three-dimensional optimal perturbations in viscous shear flows," Phys. Fluids A **4**, 1637 (1992).

[21] B. F. Farrell and P. J. Ioannou, "Optimal excitation of three-dimensional perturbations in viscous constant shear flows," Phys. Fluids A **5**, 1390–1400 (1993).

[22] K. M. Butler and B. F. Farrell, "Optimal perturbations and streak spacing in wall-bounded turbulent shear flow," Phys. Fluids A **5**, 774 (1993).

[23] H. Vitoshkin, E. Heifetz, A. Y. Gelfgat, and N. Harnik, "On the role of vortex stretching in energy optimal growth of three dimensional perturbations on plane parallel shear flows," J. Fluid Mech. **707**, 369–380 (2012).

[24] P. J. Schmid and D. S. Henningson, "A new mechanism for rapid transition involving a pair of oblique waves," Phys. Fluids A **4**, 1986–1989 (1992).

[25] G. Kreiss, A. Lundbladh, and D. S. Henningson, "Bounds for threshold amplitudes in subcritical shear flows," J. Fluid Mech. **270**, 175–198 (1994).

[26] S. C. Reddy, P. J. Schmid, J. S. Baggett, and D. S. Henningson, "On stability of streamwise streaks and transition thresholds in plane channel flows," J. Fluid Mech. **365**, 269–303 (1998).

[27] Y. Duguet, L. Brandt, and B. R. J. Larsson, "Towards minimal perturbations in plane Couette flow," Phys. Rev. E **82**, 026316 (2010).

[28] J. S. Chapman, "Subcritical transition in channel flow," J. Fluid Mech. **451**, 35–97 (2002).

[29] T. M. Schneider, B. Eckhardt, and J. A. Yorke, "Turbulence transition and the edge of chaos in pipe flow," Phys. Rev. Lett. **99**, 034502 (2007).

[30] F. Waleffe and J. Wang, *Non-Uniqueness of Solutions to the Navier-Stokes Equation and Their Connection With Laminar-Turbulent Transition*, edited by T. M. Mullin and R. R. Kerswell (Springer-Verlag, Dordrecht, 2005).

[31] F. Waleffe, "On a self-sustaining process in shear flows," Phys. Fluids **9**, 883–900 (1997).

[32] B. Hof, A. Juel, and T. M. Mullin, "Scaling of the turbulence transition threshold in a pipe," Phys. Rev. Lett. **91**, 244502 (2003).

[33] J. Cohen, J. Philip, and G. Ben-Dov, "Aspects of linear and nonlinear instabilities leading to transition in pipe and channel flows," Philos. Trans. R. Soc. London, Ser. A **367**, 509–527 (2009).

[34] F. Mellibovsky and A. Meseguer, "Critical threshold in pipe flow," Philos. Trans. R. Soc. London, Ser. A **367**, 545–560 (2009).

[35] G. Lemoult, J.-L. Aider, and J. E. Wesfreid, "Experimental scaling for the subcritical transition to turbulence in plane Poiseuille flow," Phys. Rev. E **85**, 025303(R) (2012).

[36] J. Peixinho and T. Mullin, "Finite-amplitude thresholds for transition in pipe flow," J. Fluid Mech. **582**, 169–178 (2007).

[37] T. M. Mullin, "Experimental studies of transition to turbulence in a pipe," Annu. Rev. Fluid Mech. **43**, 1–24 (2011).

[38] C. C. T. Pringle and R. R. Kerswell, "Using nonlinear transient growth to construct the minimal seed for shear flow turbulence," Phys. Rev. Lett. **105**, 154502 (2010).

[39] S. Cherubini, T. P. D. De Palma, J.-C. Robinet, and A. Bottaro, "The minimal seed of transition in the boundary layer," J. Fluid Mech. **689**, 221–253 (2011).

[40] S. Cherubini, P. D. De Palma, J.-C. Robinet, and A. Bottaro, "Rapid path to transition via nonlinear localized optimal perturbations in a boundary layer flow," Phys. Rev. E **82**, 066302 (2010).

[41] C. C. T. Pringle, A. P. Willis, and R. R. Kerswell, "Minimal seeds for shear flow turbulence: Using nonlinear transient growth to touch the edge of chaos," J. Fluid Mech. **702**, 415–443 (2012).

[42] A. Monokrousos, A. Bottaro, L. Brandt, A. Di Vita, and D. S. Henningson, "Non-equilibrium thermodynamics and the optimal path to turbulence in shear flows," Phys. Rev. Lett. **106**, 134502 (2011).

[43] W. V. R. Malkus, "Outline of a theory of turbulent shear flow," J. Fluid Mech. **1**, 521–539 (1956).

[44] S. M. E. Rabin, C. P. Caulfield, and R. R. Kerswell, "Variational identification of minimal seeds to trigger transition in plane Couette flow," J. Fluid Mech. **712**, 244–272 (2012).

[45] S. Cherubini and P. D. De Palma, "Nonlinear optimal perturbations in a Couette flow," J. Fluid Mech. **716**, 251–279 (2013).

[46] M. Chevalier, P. Schlatter, A. Lundbladh, and D. S. Henningson, "SIMSON: A pseudo-spectral solver for incompressible boundary layer flows," Technical Report No. TRITA-MEK 2007:07, KTH Mechanics, Stockholm, Sweden, 2007.

[47] A. Monokrousos, E. Åkervik, L. Brandt, and D. S. Henningson, "Global optimal disturbances in the Blasius boundary-layer flow using time-steppers," J. Fluid Mech. **650**, 181–214 (2010).

[48] G. D. Chagelishvili, R. G. Chanishvili, and D. G. Lominadze, "Physics of the amplification of vortex disturbances in shear flows," JETP Lett. **63**, 543–549 (1996).

[49] C. Cossu, L. Brandt, S. Bagheri, and D. S. Henningson, "Secondary threshold amplitudes for sinuous streak breakdown," Phys. Fluids **23**, 074103 (2011).

[50] L. Brandt and H. C. D. De Lange, "Streak interaction and breakdown in boundary layer flows," Phys. Fluids **20**, 024107 (2008).

[51] P. Andersson, L. Brandt, A. Bottaro, and D. S. Henningson, "On the breakdown of boundary layer streaks," J. Fluid Mech. **428**, 29–60 (2001).

[52] G. Kawahara, J. Jimenez, M. Uhlmann, and A. Pinelli, "Linear instability of a corrugated vortex sheet: A model for streak instability," J. Fluid Mech. **483**, 315–342 (2003).

[53] C. Cossu, M. P. Chevalier, and D. S. Henningson, "Optimal secondary growth in a plane channel flow," Phys. Fluids **19**, 058107 (2007).

[54] J. A. Vastano and R. D. Moser, "Short-time Lyapunov exponent analysis and the transition to chaos in Taylor-Couette flow," J. Fluid Mech. **233**, 83–118 (1991).

[55] Y. Duguet, A. P. Willis, and R. R. Kerswell, "Transition in pipe flow : The saddle structure on the boundary of turbulence," J. Fluid Mech. **613**, 255–274 (2008).

[56] D. Viswanath, "The dynamics of transition to turbulence in plane Couette flow," in *Mathematics and Computation, a Contemporary View: The Abel Symposium* (Springer-Verlag, Berlin, 2008).

[57] D. Viswanath, "The critical layer in pipe flow at high Reynolds number," Philos. Trans. R. Soc. London, Ser. A **367**, 561–576 (2009).

[58] J. Vollmer, T. M. Schneider, and B. Eckhardt, "Basin boundary, edge of chaos and edge state in a two-dimensional model," New J. Phys **11**, 013040 (2009).

[59] L. Brandt, "Numerical studies of the instability and breakdown of a boundary-layer low-speed streak," Eur. J. Mech. B/Fluids **26**, 64–82 (2007).

[60] R. Takaki, "Spanwise propagation of turbulence in the plane Couette flow," Fluid Dyn. Res. **1**, 229–236 (1987).

[61] Y. Duguet, O. Le Maître, and P. Schlatter, "Stochastic and deterministic motion of a laminar-turbulent front in a spanwisely extended Couette flow," Phys. Rev. E **84**, 066315 (2011).

[62] A. Lundbladh and A. V. Johansson, "Direct simulation of turbulent spots in plane Couette flow," J. Fluid Mech. **229**, 499–516 (1991).

[63] Y. Duguet, P. Schlatter, and D. S. Henningson, "Localized edge states in plane Couette flow," Phys. Fluids **21**, 111701 (2009).

[64] T. M. Schneider, D. Marinc, and B. Eckhardt, "Localized edge states nucleate turbulence in plane Couette cells," J. Fluid Mech. **646**, 441–451 (2010).